POLITECNICO DI TORINO
Repository ISTITUZIONALE

On the Vibration Analysis of Coupled Transverse and Shear Piezoelectric FG Porous Beams with
Higher-Order Theories

(Article begins on next page)

04 August 2020

On the Vibration Analysis of Coupled Transverse and Shear Piezoelectric FG Porous Beams with Higher-Order Theories

M. Askari, E. Brusa, C. Delprete

Department of Mechanical and Aerospace Engineering (DIMEAS), Politecnico di Torino, Corso Duca degli Abruzzi, 24, 10129 Torino, Italy

Abstract

This investigation aims to perform a detailed natural frequency analysis of functionally graded porous beams integrated with transverse (d_{31}) and shear (d_{15}) piezoelectric layers under short circuit (SC) and open circuit (OC) electrical conditions. It is assumed that the core layer is made of functionally graded materials (FGMs) containing porosities. Due to the existence of internal pores, the mechanical properties of FGMs are considered according to the modified power-law rule which includes the effect of porosity. The distribution of electric potential within the d_{31} and d_{15} piezoelectric layers is modeled based on nonlinear variation for both SC and OC conditions. Employing the classical, the first-order and the higher-order beam theories incorporated with the virtual work principle as well as the Maxwell's equation, the electromechanical equations of motion are derived. The governing equations are then solved analytically for simply supported boundary condition and a parametric study is presented. After validation of the results, some new interesting conclusions covering the effects of porosity volume fraction, porosity distribution, various piezoelectricity modes, power-law index and the beam theories on SC and OC resonance frequencies are reported. It is believed that the presented numerical results could provide a benchmark to check the accuracy of the approximated approaches.

1. Introduction

As it is well-known, functionally graded materials (FGMs) are novel emerging class of composites within which material properties such as elasticity modulus and mass density vary continuously over the volume in one or more directions. The most familiar FGM is generally made of a mixture of ceramics and metals in which the ceramic constituent exhibits high heat resistance due to its low thermal conductivity, and the metal component provides large mechanical strength to resist the failure of structures. One of the most important benefits of FGMs against the typical laminated composites is that FGMs represent smooth and continuous variations in the material properties enabling them to be excellent solutions to avoid delamination and propagation of cracks which can be occurred due to large interlaminar stresses and plastic deformations[1]. Having these properties, FGMs have been attracted attention as potential materials for a wide range of applications in aerospace, energy conversion, engine components, electronics, biomedical, and optics[1, 2]. Over the past decades, hundreds of works have been done to investigate mechanical behaviors of FGM structures. For detailed investigations of structural members made of FGMs, one may see[3-16] and many other works presented in the related literature.

Various special methods such as chemical and physical deposition, powder stacking, plasma spraying and sintering have been used to fabricate FGMs. However, it is recently reported that in production of FGMs, internal porosities may appear inside the material structure due to the huge difference between the solidification temperatures of the material constituents during the sintering process[17]. The existence of porosities can significantly influence the mechanical properties and the behavior of materials so that it is of concern to examine the effects of porosities on the static and dynamic behavior of engineering structures made of FGMs. Wattanasakulpong et al.[18] discussed the effects of the internal porosities which appear in FGM samples manufactured within a multi-step sequential filtration method. Using Ritz's method, elastic buckling and bending analysis of functionally graded porous beams is studied by Chen et al.[19] based on Timoshenko's beam theory. The same authors[20] investigated nonlinear free vibration of a sandwich beam with functionally graded core having different types of porosity distribution. Ebrahimi and his colleagues[21-23] developed numerical and semi-analytical solutions to study the vibrational behavior of functionally graded porous structures using the classical and the first-order shear theories. They investigated the effects of various types of porosity distributions as well as thermal loadings on the natural frequencies of the systems. Recently, Wang and co-authors[24, 25] conducted research studies on the nonlinear vibration of FGM rectangular plates with porosities moving in thermal environment and contacting with liquid. In their works, they assumed the geometrical nonlinearity based on von Karman nonlinear theory and used the Galerkin's method to solve the governing equations of motion. Nonlinear free vibration of metal foam cylindrical shells, and forced vibration analysis of functionally graded piezoelectric plates containing porosities were carried out by Wang et al.[26, 27], in which the harmonic balance method and Galerkin's approach are employed to solve the governing equations and extract the numerical results. Also, bending analysis of single-layered and sandwich plates made of FGMs with porosities is investigated by Zenkour[28] based on a quasi-3D refined shear deformation theory. Nguyen et al.[29] carried out the study of linear and nonlinear static and dynamic responses of porous FGM plates using an efficient polygonal finite element method. Very recently, Wang and Zhao studied bending, buckling and vibration of shear deformable porous beams by means of the Navier's approach as well as Rayleigh-Ritz's method for various boundary conditions[30].

On the other hand, intelligent materials, particularly piezoelectrics, have been widely integrated with structural systems to use in engineering applications such as vibration control, energy harvesting, medicine, space and many others[31-35]. Piezoelectrics have the capability of generating electricity when subjected to mechanical stress and strain fields, and vice versa, known as direct and converse piezoelectric effects, respectively. Having these peculiar features, piezoelectric materials are potential candidates for developing smart structures with self-monitoring and self-controlling capabilities. However, due to the superior thermo-mechanical properties of FGMs, by integrating piezoelectric materials onto the FGM structures, smart functionally graded structural systems are produced which can be used for different purposes such as active vibration suppression, energy harvesting and shape control[32-39]. Thus, the interaction between the FGM host structures and piezoelectric patches/layers should be well understood to effectively utilize the properties of piezoelectrics. Over the last years, some researchers have focused their attention on studying the mechanical response of FGM structures with surface-mounted piezoelectric layers/patches due to the increasing use of smart materials in vibration control. One of the primary studies on smart FGM structures was carried out by Reddy and Cheng[40] to present 3D solutions for FGM plates integrated with actuator layers made of piezoelectric materials. Wang and Noda[41] developed a finite element code for the analysis of a smart FGM composite structure composed of an FGM core sandwiched between a metal layer and a piezoelectric

layer used as an actuator. Huang and Shen[42] investigated thermomechanical nonlinear vibration and dynamic response of simply-supported FGM plates with two piezoelectric layers mounted on its top and bottom surfaces using higher-order shear deformation theory. Based on Timoshenko's beam theory, Kiani et al.[43] conducted thermo-electrical buckling analysis of FGM beams with or without piezoelectric layers subjected to both thermal loading and electrical field. Askari Farsangi and co-authors[44, 45] developed analytical solutions to study the free vibration of coupled piezoelectric FGM plates based on different plate models. Wang[46] investigated the electro-mechanical characteristics of functionally graded piezoelectric plates having porosities in translation state.

In view of the above, studies on vibration analysis of FGM beams integrated with piezoelectric layers are relatively less compared to smart FGM plates and shells. To the best of authors' knowledge, no work has been presented for the free vibration analysis of thick FGM beams containing porosities surrounded by various types of piezoelectric layers based on higher-order shear theories. Concerning practical application of piezoelectric materials in sensor and actuator technologies, piezoelectric motors etc., it could be useful to carry out the above-mentioned topic to provide a benchmark for further application of piezoelectric materials and structures.

In this paper, the classical and the higher-order theories are used to analytically study the effects of both d_{31} and d_{15} piezoelectric layers as well as different types of porosity distribution on the natural frequencies of thick smart functionally graded porous (FGP) beams, under both SC and OC electrical conditions. A nonlinear model is used for the distribution of electric potential through the piezoelectric layers. The material properties of the substrate layer are assumed to be graded across its thickness based on two different patterns, namely even and uneven distribution. Using the Hamilton's principle and the Maxwell's electrostatic equation, the governing equations of motion and the associated boundary conditions (BC's) are derived for both SC and OC conditions. An exact solution based on Navier's method is then employed to solve the governing equations for hybrid beams. After validating the presented formulation, the effects of materials properties, porosity parameter, power-law index, geometry dimensions and piezoelectric characteristics on the beam natural frequencies are examined in details, and comparisons are made among various beam theories.

2. Kinematics modeling

The layouts of the considered FGP beams embedded with d_{31} and d_{15} piezoelectric layers are shown in Figures 1(a) and 1(b), respectively. The origin of the Cartesian reference system is located in the mid-plane of the core layer. L, b, $2t_c$ and t_p are the length, width, core thickness and each piezoelectric layer's thickness of the sandwich beam, respectively. It is assumed that in each of the two cases, the sandwich beam consists of a functionally graded core having porosities inside its structure, and two piezoelectric layers which are symmetrically bonded on the top and bottom faces of the core layer. The bonded piezoelectric layers are considered to be made of transversely piezoelectric materials which are polarized in the thickness and the axial directions of the beam for d_{31} and d_{15} piezoelectricity modes, respectively.

(a) d_{31} Mode
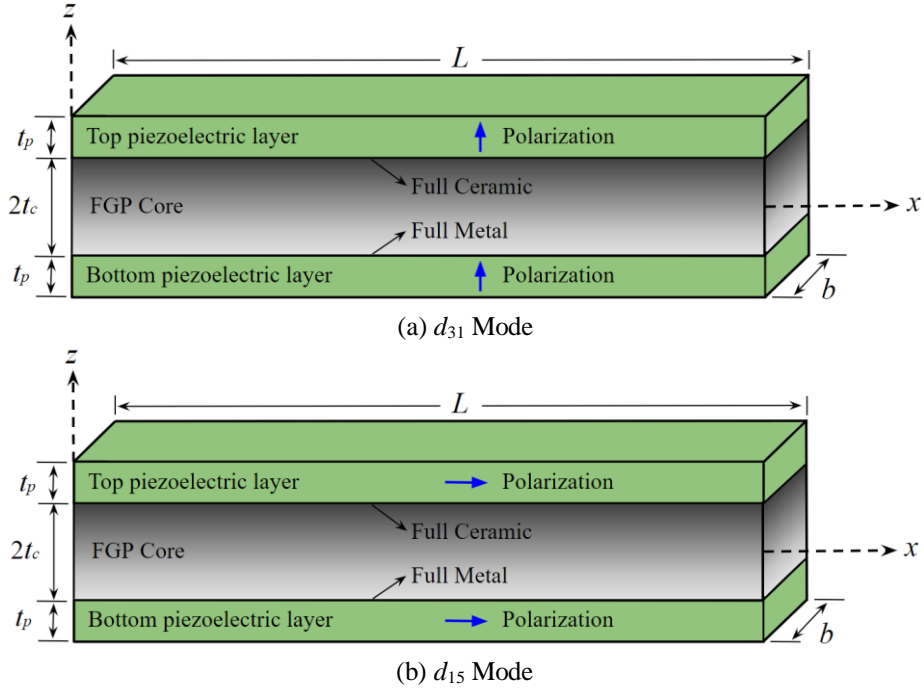
(b) d_{15} Mode

Figure 1. Layouts of the beams made of FGMs with porosities surrounded by piezoelectric layers in d_{31} and d_{15} modes

Mechanical properties of FGMs including porosities are assumed to vary smoothly along the beam thickness. Two different patterns of porosity, namely even and uneven, are considered to describe the distribution of the internal pores which are occurred inside the structure of FGMs due to defects in manufacturing process. Thus, the effective mechanical properties such as Young's modulus $E(z)$ and mass density $\rho(z)$ are modeled based on the modified rule of mixture, as recently presented in literature[21, 24, 47, 48]:

$$
\begin{cases}
E(z) = E_m + (E_c - E_m)\left(\dfrac{1}{2} + \dfrac{z}{2t_c}\right)^k - \dfrac{\alpha}{2}(E_c + E_m) \\[3mm]
\rho(z) = \rho_m + (\rho_c - \rho_m)\left(\dfrac{1}{2} + \dfrac{z}{2t_c}\right)^k - \dfrac{\alpha}{2}(\rho_c + \rho_m)
\end{cases}
\tag{1a}
$$

$$
\begin{cases}
E(z) = E_m + (E_c - E_m)\left(\dfrac{1}{2} + \dfrac{z}{2t_c}\right)^k - \dfrac{\alpha}{2}\left(1 - \dfrac{|z|}{t_c}\right)(E_c + E_m) \\[3mm]
\rho(z) = \rho_m + (\rho_c - \rho_m)\left(\dfrac{1}{2} + \dfrac{z}{2t_c}\right)^k - \dfrac{\alpha}{2}\left(1 - \dfrac{|z|}{t_c}\right)(\rho_c + \rho_m)
\end{cases}
\tag{1b}
$$

where the positive real number k ($0 \leq k < \infty$) and the parameter α ($0 \leq \alpha < 1$) show the power-law index and the porosity volume fraction of FGMs, respectively. Besides, the subscripts m and c represent the corresponded material properties of metal and ceramic parts of the FGP core, respectively.

From Equation (1), it is clear that when the value of k is equal to zero, we have a fully ceramic beam and setting k to large values presents the properties of a beam completely made of metal. However, the material properties of a homogenous beam with no porosity can be obtained when $\alpha = k = 0$. It should be noted that Equation (1a) is associated with the properties of FGMs with even porosity

distribution, while those corresponded to FGMs with unevenly distributed pores are described in Equation 1(b). In Figure (2), these two patterns of porosities throughout the beam cross-section are shown schematically for illustrative purposes. It seems from Figure (2b) that in uneven pattern, the internal pores are mostly distributed in the middle area of the beam cross-section and the amount of porosity tends to linearly drop to zero at the top and bottom areas of the beam cross-section. According to the fundamental of multi-step infiltration process which can be employed to fabricate FGM samples, most of the internal pores occur in the middle region[21]. This is due to the reason that it is not easy to totally infiltrate the materials in this area, whilst at the top and bottom zones, the infiltration process of material could be carried out easier and less porosities are then appeared[49].

(a) Even porosity pattern   (b) Uneven porosity pattern
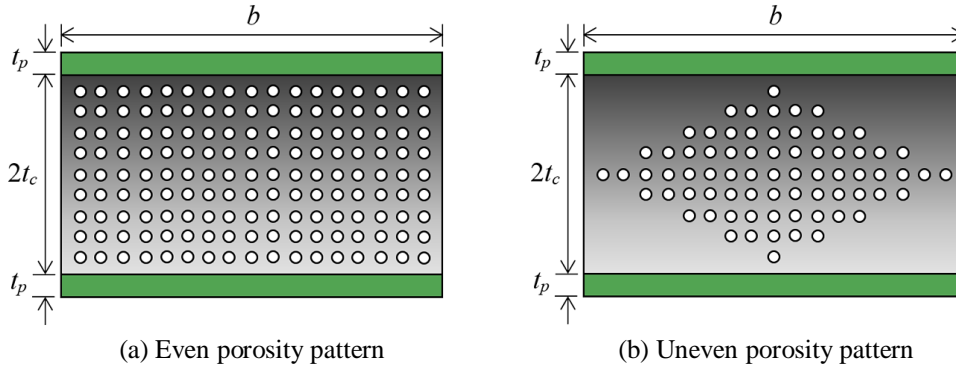
Figure 2. Distribution of the internal pores within the cross-section of the smart FGP beam

Using piezoelectric materials in various operation modes leads to different electromechanical behaviors due to their different piezoelectric coupling coefficients. The shear mode is actually corresponded with the shear deformation of the piezoelectric layers, when they are polarized in the axial direction of the beam. Therefore, to provide an accurate prediction, the effects of transverse shear deformation on the system behavior must be considered when analyzing piezoelectrics in shear mode[50]. In this study, the mechanical displacement field is modeled according to Equation (2) in order to consider the shear deformation effects based on various higher-order beam theories[9]:

$$u(x,z,t) = u_0(x,t) - z \frac{\partial w_0(x,t)}{\partial x} + f(z)\psi(x,t)$$
$$v(x,z,t) = 0$$
$$w(x,z,t) = w_0(x,t)$$

(2)

in which $u_0(x,t)$ and $w_0(x,t)$ are the axial and transverse displacement components of the mid-plane of the beam along x- and z-axes, respectively; $\psi(x,t)$ is the rotation function of transverse normal of the mid-plane (at $z=0$). The parameter t shows time variable and $f(z)$ is the shape function representing the effect of the transverse shear strain and stress along the thickness of the beam. For comparative purposes, various applicable shape functions[51] corresponded to different beam displacement models and theories are employed in this study as listed in Table 1.

Table 1. Various shape functions for different beam theories

Theory	Shape Function
Classical Beam Theory (CBT)	$f(z) = 0$

First-order Shear Deformation Beam Theory (FBT)	$f(z) = z$
Parabolic Shear Deformation Beam Theory (PBT)	$f(z) = z\left[1 - \dfrac{4}{3}\left(\dfrac{z}{2t_c + 2t_p}\right)^2\right]$
Sinusoidal Shear Deformation Beam Theory (SBT)	$f(z) = \dfrac{2t_c + 2t_p}{\pi}\sin\left(\dfrac{\pi z}{2t_c + 2t_p}\right)$
Exponential Shear Deformation Beam Theory (EBT)	$f(z) = z\exp\left[-2\left(\dfrac{z}{2t_c + 2t_p}\right)^2\right]$

Using the linear strain-displacement relationship, the components of the strain field for the sandwich beam can be derived from Equation (2) as follows:

$$\varepsilon_{xx}(x,z,t) = \frac{\partial u}{\partial x} = \frac{\partial u_0}{\partial x} - z\frac{\partial^2 w_0}{\partial x^2} + f(z)\frac{\partial \psi}{\partial x}$$

$$\gamma_{xz}(x,z,t) = \frac{\partial u}{\partial z} + \frac{\partial w}{\partial x} = f'(z)\psi$$

$$\varepsilon_{yy}(x,z,t) = \frac{\partial v}{\partial y} = 0$$

$$\gamma_{xy}(x,z,t) = \frac{\partial u}{\partial y} + \frac{\partial v}{\partial x} = 0 \qquad (3)$$

$$\varepsilon_{zz}(x,z,t) = \frac{\partial w}{\partial z} = 0$$

$$\gamma_{yz}(x,z,t) = \frac{\partial v}{\partial z} + \frac{\partial w}{\partial y} = 0$$

It is noted that in CBT, since $f(z)=0$, the value of γ_{xz} is equal to zero at any point of the beam. It means that the transverse shear deformation is neglected in CBT which leads to make this approach unsuitable for analyzing relatively thick and thick beams, unlike higher order theories.

3. Materials modelling and constitutive equations

3.1. Piezoelectric layers in d_{31} and d_{15} modes

In the current study, the piezoelectric materials are assumed to be homogenous and transversely isotropic, with the z and x axes as the axes of isotropy in d_{31} and d_{15} operation modes, respectively. The general constitutive equations for the transverse piezoelectric mode are taken to be[52]:

$$
\begin{Bmatrix}
\sigma_{xx}^{31} \\
\sigma_{yy}^{31} \\
\sigma_{zz}^{31} \\
\sigma_{yz}^{31} \\
\sigma_{xz}^{31} \\
\sigma_{xy}^{31} \\
D_{x}^{31} \\
D_{y}^{31} \\
D_{z}^{31}
\end{Bmatrix}
=
\begin{bmatrix}
C_{11} & C_{12} & C_{13} & 0 & 0 & 0 & 0 & 0 & -e_{31} \\
C_{12} & C_{11} & C_{13} & 0 & 0 & 0 & 0 & 0 & -e_{31} \\
C_{13} & C_{13} & C_{33} & 0 & 0 & 0 & 0 & 0 & -e_{33} \\
0 & 0 & 0 & C_{55} & 0 & 0 & 0 & -e_{15} & 0 \\
0 & 0 & 0 & 0 & C_{55} & 0 & -e_{15} & 0 & 0 \\
0 & 0 & 0 & 0 & 0 & C_{66} & 0 & 0 & 0 \\
0 & 0 & 0 & 0 & 0 & 0 & \Xi_{11} & 0 & 0 \\
0 & 0 & 0 & 0 & 0 & 0 & 0 & \Xi_{11} & 0 \\
e_{31} & e_{31} & e_{33} & 0 & 0 & 0 & 0 & 0 & \Xi_{33}
\end{bmatrix}
\begin{Bmatrix}
\varepsilon_{xx} \\
\varepsilon_{yy} \\
\varepsilon_{zz} \\
\gamma_{yz} \\
\gamma_{xz} \\
\gamma_{xy} \\
E_{x} \\
E_{y} \\
E_{z}
\end{Bmatrix}
\tag{4}
$$

where σ_{ij}, ε_{ij}, γ_{ij}, D_i and E_i represent mechanical stress, normal strain, shear strain, electric displacement and electric field components, respectively. The piezoelectric material properties of C_{ij}, e_{ij} and Ξ_{ij} are also stiffness, electromechanical coupling and permittivity coefficients, respectively. Furthermore, the interaction between mechanical and electrical fields in the shear piezoelectric mode can be extracted from Equation (4) through a 90º rotation around the *y*-direction, followed by a 180º rotation around the *z*-direction[50]. By applying these rotations to the above relation, the electromechanical constitutive equations in the shear operation mode can be expressed as:

$$
\begin{Bmatrix}
\sigma_{xx}^{15} \\
\sigma_{yy}^{15} \\
\sigma_{zz}^{15} \\
\sigma_{yz}^{15} \\
\sigma_{xz}^{15} \\
\sigma_{xy}^{15} \\
D_{x}^{15} \\
D_{y}^{15} \\
D_{z}^{15}
\end{Bmatrix}
=
\begin{bmatrix}
C_{33} & C_{13} & C_{13} & 0 & 0 & 0 & -e_{33} & 0 & 0 \\
C_{13} & C_{11} & C_{12} & 0 & 0 & 0 & -e_{31} & 0 & 0 \\
C_{13} & C_{12} & C_{11} & 0 & 0 & 0 & -e_{31} & 0 & 0 \\
0 & 0 & 0 & C_{66} & 0 & 0 & 0 & 0 & 0 \\
0 & 0 & 0 & 0 & C_{55} & 0 & 0 & 0 & -e_{15} \\
0 & 0 & 0 & 0 & 0 & C_{55} & 0 & -e_{15} & 0 \\
e_{33} & e_{31} & e_{31} & 0 & 0 & 0 & \Xi_{33} & 0 & 0 \\
0 & 0 & 0 & 0 & 0 & e_{15} & 0 & \Xi_{11} & 0 \\
0 & 0 & 0 & 0 & e_{15} & 0 & 0 & 0 & \Xi_{11}
\end{bmatrix}
\begin{Bmatrix}
\varepsilon_{xx} \\
\varepsilon_{yy} \\
\varepsilon_{zz} \\
\gamma_{yz} \\
\gamma_{xz} \\
\gamma_{xy} \\
E_{x} \\
E_{y} \\
E_{z}
\end{Bmatrix}
\tag{5}
$$

It should be mentioned that here and hereafter, the superscripts 31 and 15 denote the corresponding variables for the transverse and shear modes of piezoelectric layers, respectively. From Equations (4) and (5), it can be easily seen that the electromechanical relationships between stress and strain components as well as mechanical and electrical properties of piezoelectric materials are highly dependent on the polarization direction. Thus, these differences in the constitutive equations result in different electromechanical behaviors when using piezoelectric materials in transverse and shear modes.

Approximation of the electric potential variation ϕ through the piezoelectric layers is an important issue. In this study, the electric potential is assumed to have a nonlinear variation along the thickness of piezoelectric layers for both transverse and shear modes as well as SC and OC conditions, as proposed in[53, 54]. Furthermore, in each operation mode, two common electrical circuit conditions (i.e. SC and OC conditions) are considered. It is known that in the SC condition, both inner and outer surfaces of each piezoelectric layer are held at zero electric voltage, $\phi(x,\pm t_c,t) = \phi\big(x,\pm(t_c +$

$t_p),t) = 0$. On the other hand, applying these conditions only on the outer surfaces and electrically insulating the inner surfaces of each piezoelectric layer result in the OC electrical condition, $\phi(x,\pm t_c,t) = D_z(x,\pm(t_c + t_p),t) = 0$. Concerning these conditions, the electric potential function through the piezoelectric layers is first assumed to have the following nonlinear form with respect to z-coordinate[53, 54]:

$$\phi(x,z,t) = \begin{cases} \phi_0(x,t)\left[1 - \left(\dfrac{+2z - 2t_c - t_p}{t_p}\right)^2\right] + Az + B & t_c \leq z \leq t_c + t_p \\[3em] \phi_0(x,t)\left[1 - \left(\dfrac{-2z - 2t_c - t_p}{t_p}\right)^2\right] + Cz + D & -t_c - t_p \leq z \leq -t_c \end{cases} \tag{6}$$

where $\phi_0(x,t)$ is the electric potential distribution in the mid-plane of each piezoelectric layer. Also, A, B, C and D are four unknown functions of the x-coordinate and time variable which should be determined satisfying the electrical BC's corresponded to each of SC and OC electrical conditions.

Applying these conditions to Equation (6), the final form of the electric potential function is obtained as follows:

For the top piezoelectric layer ($t_c \leq z \leq t_c + t_p$):

$$\begin{aligned} \phi(x,z,t) = \phi_0(x,t)&\left[1 - \left(\frac{+2z - 2t_c - t_p}{t_p}\right)^2\right] \\ &+ (z - t_c)\left[\alpha_1\left(\frac{4}{t_p}\phi_0(x,t) + \frac{e_{15}\zeta_1}{\Xi_{11}}\psi(x,t)\right)\right. \\ &\left. + \alpha_2\left(\frac{4}{t_p}\phi_0(x,t) + \frac{e_{31}}{\Xi_{33}}\frac{\partial u_0}{\partial x} - \frac{e_{31}(h + h_p)}{\Xi_{33}}\frac{\partial^2 w_0}{\partial x^2} + \frac{e_{31}\eta_1}{\Xi_{33}}\frac{\partial \psi}{\partial x}\right)\right] \end{aligned} \tag{7}$$

For the bottom piezoelectric layer ($-t_c - t_p \leq z \leq -t_c$):

$$\begin{aligned} \phi(x,z,t) = \phi_0(x,t)&\left[1 - \left(\frac{-2z - 2t_c - t_p}{t_p}\right)^2\right] \\ &+ (z + t_c)\left[\alpha_3\left(\frac{-4}{t_p}\phi_0(x,t) + \frac{e_{15}\zeta_2}{\Xi_{11}}\psi(x,t)\right)\right. \\ &\left. + \alpha_4\left(\frac{-4}{t_p}\phi_0(x,t) + \frac{e_{31}}{\Xi_{33}}\frac{\partial u_0}{\partial x} + \frac{e_{31}(h + h_p)}{\Xi_{33}}\frac{\partial^2 w_0}{\partial x^2} + \frac{e_{31}\eta_2}{\Xi_{33}}\frac{\partial \psi}{\partial x}\right)\right] \end{aligned} \tag{8}$$

where the coefficients α_i ($i = 1, 2, 3, 4$) can only be equal to zero ($\alpha_i = 0$) and unit number ($\alpha_i = 1$) for the studied piezoelectric modes and electrical circuit conditions as given in Table 2. Furthermore, the coefficients $\zeta_1 = f'(z = t_c + t_p)$, $\zeta_2 = f'(z = -t_c - t_p)$, $\eta_1 = f(z = t_c + t_p)$ and $\eta_2 = f(z = -t_c - t_p)$ have different values for each mechanical displacement field, since f and f' are the shape function (listed in Table 1) and its derivative with respect to the z-coordinate, respectively.

Table 2. Values of the parameters α_i ($i = 1, 2, 3, 4$) for various piezoelectric modes and electrical boundary conditions

Piezoelectric layers (Electrical Circuit Condition)	α_1	α_2	α_3	α_4
d_{31} Mode (SC)	0	0	0	0
d_{31} Mode (OC)	0	1	0	1
d_{15} Mode (SC)	0	0	0	0
d_{15} Mode (OC)	1	0	1	0

Using the electric potential functions from Equations (7) and (8), the components of the electric field in piezoelectric layers could be derived from the following equation:

$$[E_x, E_y, E_z] = -\left[\frac{\partial\phi}{\partial x}, \frac{\partial\phi}{\partial y}, \frac{\partial\phi}{\partial z}\right]$$

(9)

3.2. Functionally graded core with porosities

Since FGMs are isotropic materials, they simply obey the Hooke's law and their constitutive equations can be expressed in the following general form[44]:

$$\begin{Bmatrix} \sigma_{xx}^c \\ \sigma_{yy}^c \\ \sigma_{yz}^c \\ \sigma_{xz}^c \\ \sigma_{xy}^c \end{Bmatrix} = \begin{bmatrix} Q_{11} & Q_{12} & 0 & 0 & 0 \\ Q_{12} & Q_{11} & 0 & 0 & 0 \\ 0 & 0 & Q_{44} & 0 & 0 \\ 0 & 0 & 0 & Q_{55} & 0 \\ 0 & 0 & 0 & 0 & Q_{66} \end{bmatrix} \begin{Bmatrix} \varepsilon_{xx} \\ \varepsilon_{yy} \\ \gamma_{yz} \\ \gamma_{xz} \\ \gamma_{xy} \end{Bmatrix}$$

(10)

where the elastic coefficients Q_{ij} are defined as $Q_{11} = E(z)/(1 - \nu^2)$, $Q_{12} = \nu Q_{11}$ and $Q_{44} = Q_{55} = Q_{66} = E(z)/(2 + 2\nu)$ in which ν is the Poisson ratio. Here and hereafter, the superscript c represents the corresponding variables for the core layer of the coupled smart beam.

4. Electromechanical equations of motion

Based on the Hamilton's principle, the equations of motion for the free vibration problem can be derived using the following relation:

$$\int_{t_0}^{t_1} (\delta U - \delta K)\, dt = 0$$

(11)

in which δ denotes the variational operator, and δU and δK are the variation of the strain and kinetic energy of the system.

In the Equation (11), the energy variations δU and δK can be calculated with the help of Equations (2) and (3) as follows:

$$\int_{t_0}^{t_1} \delta U \, dt = \int_{t_0}^{t_1} \int_V \sigma_{ij} \delta \varepsilon_{ij} \, dV dt = \int_{t_0}^{t_1} \int_0^L \int_0^b \int_{-t_c-t_p}^{+t_c+t_p} (\sigma_{xx} \delta \varepsilon_{xx} + \sigma_{xz} \delta \gamma_{xz}) \, dz dy dx dt \qquad (12a)$$

$$\int_{t_0}^{t_1} \delta K \, dt = \int_{t_0}^{t_1} \int_0^L \int_0^b \int_{-t_c-t_p}^{+t_c+t_p} \rho \left[\frac{\partial u}{\partial t} \delta \left(\frac{\partial u}{\partial t} \right) + \frac{\partial w}{\partial t} \delta \left(\frac{\partial w}{\partial t} \right) \right] \, dz dy dx dt \qquad (12b)$$

where ρ is the effective mass density of the sandwich beam.

Substituting the strain and kinetic energy variations into the Hamilton's principle and applying several integrations by parts, the electromechanical equations of motion for the beam are obtained as follows:

$$\delta u_0: \qquad \frac{\partial N_{xx}^{pq}}{\partial x} - I_0 \frac{\partial^2 u_0}{\partial t^2} - I_{01} \frac{\partial^2 \psi}{\partial t^2} + I_1 \frac{\partial^3 w_0}{\partial x \partial t^2} = 0 \qquad (13a)$$

$$\delta w_0: \qquad \frac{\partial^2 M_{xx}^{pq}}{\partial x^2} - I_1 \frac{\partial^3 u_0}{\partial x \partial t^2} - I_{11} \frac{\partial^3 \psi}{\partial x \partial t^2} - I_0 \frac{\partial^2 w_0}{\partial t^2} + I_2 \frac{\partial^4 w_0}{\partial x^2 \partial t^2} = 0 \qquad (13b)$$

$$\delta u_1: \qquad \frac{\partial \widehat{M}_{xx}^{pq}}{\partial x} - \widehat{Q}_{xz}^{pq} - I_{01} \frac{\partial^2 u_0}{\partial t^2} - I_{02} \frac{\partial^2 \psi}{\partial t^2} + I_{11} \frac{\partial^3 w_0}{\partial x \partial t^2} = 0 \qquad (13c)$$

where N_{xx}, M_{xx}, $\widehat{M}_{xx}$ and $\widehat{Q}_{xz}$ are the stress resultants. It should be noted that here and hereafter, the superscript *pq* represents the associated variables and coefficients for the transverse and shear modes of piezoelectric materials so that it can only be equal to 31 and 15 for d_{31} and d_{15} piezoelectricity modes, respectively. For instance, when *pq* is equal to 31, it does mean that the constitutive equations corresponded to d_{31} mode (given in Equation (4)) must be used to determine the related coefficients and variables such as the stress resultants. Moreover, the appearance of the terms $\widehat{M}_{xx}^{pq}$ and $\widehat{Q}_{xz}^{pq}$ in Equations (13) is due to the particular form of the mechanical displacement field and they are not appeared in the equations of motion, when using the classical beam theory.

The terms I_i and I_{ij} which represent the mass inertias of the sandwich beam are defined as:

$$I_i = \int_{-t_c-t_p}^{-t_c} \rho \, z^i \, dz + \int_{-t_c}^{+t_c} \rho(z) \, z^i \, dz + \int_{+t_c}^{+t_c+t_p} \rho \, z^i \, dz, \qquad (i = 0,1,2) \qquad (14a)$$

$$I_{ij} = \int_{-t_c-t_p}^{-t_c} \rho \, z^i \, [f(z)]^j \, dz + \int_{-t_c}^{+t_c} \rho \, z^i \, [f(z)]^j \, dz + \int_{+t_c}^{+t_c+t_p} \rho \, z^i \, [f(z)]^j \, dz, \qquad (14b)$$

$$(i = 0,1 \text{ and } j = 1,2)$$

and similarly, the stress resultants are defined in terms of stress components in the following forms:

$$\left(N_{xx}^{pq}, M_{xx}^{pq} \right) = \int_{-t_c-t_p}^{-t_c} \sigma_{xx}^{pq} \, (1,z) \, dz + \int_{-t_c}^{+t_c} \sigma_{xx}^c \, (1,z) \, dz + \int_{+t_c}^{+t_c+t_p} \sigma_{xx}^{pq} \, (1,z) \, dz \qquad (15a)$$

$$\widehat{M}_{xx}^{pq} = \int_{-t_c-t_p}^{-t_c} \sigma_{xx}^{pq} \, f(z) \, dz + \int_{-t_c}^{+t_c} \sigma_{xx}^c \, f(z) \, dz + \int_{+t_c}^{+t_c+t_p} \sigma_{xx}^{pq} \, f(z) \, dz \qquad (15b)$$

$$\hat{Q}_{xz}^{pq} = \int_{-t_c-t_p}^{-t_c} \sigma_{xz}^{pq} \, f'(z) \, dz + \int_{-t_c}^{+t_c} \sigma_{xz}^{c} \, f'(z) \, dz + \int_{+t_c}^{+t_c+t_p} \sigma_{xz}^{pq} \, f'(z) \, dz \qquad (15c)$$

Moreover, from the Hamilton's principle, the following mechanical BC's at the edges $x = 0$ and $x = L$ of the beam can be obtained:

$$
\begin{array}{lll}
u_0 = 0 & \text{or} & N_{xx}^{pq} = 0 \\[4pt]
\dfrac{\partial w_0}{\partial x} = 0 & \text{or} & M_{xx}^{pq} = 0 \\[8pt]
w_0 = 0 & \text{or} & \dfrac{\partial M_{xx}^{pq}}{\partial x} = 0 \\[8pt]
\psi = 0 & \text{or} & \hat{M}_{xx}^{pq} = 0
\end{array}
\qquad (16)
$$

Generally, the left-hand side BC's in equation (16) are called essential or geometric BC's because they correspond to prescribe displacements and rotations, and must be rigorously imposed according to the beam boundaries. Besides, the right-hand side ones are called natural BC's which are associated with the loads and moment resultants acting on each end of the beam and they are implicitly contained in the Hamilton's principle. In the next section, the expressions given in relation (16) will be summarized for a particular type of mechanical BC at the beam boundaries.

Using the mechanical displacement field and strain-displacement relations given in equations (2) and (3) as well as with the help of constitutive equations (4), (5) and (10) for both piezoelectrics and FGMs, the stress resultants (15a) to (15c) can be rewritten in terms of displacement components and electric potential function as follows:

$$N_{xx}^{pq} = a_1^{pq} \frac{\partial u_0}{\partial x} + a_2^{pq} \frac{\partial^2 w_0}{\partial x^2} + a_3^{pq} \frac{\partial \psi}{\partial x} + \mu_1^{pq} \phi_0 + \beta_1^{pq} \frac{\partial \phi_0}{\partial x} \qquad (17a)$$

$$M_{xx}^{pq} = a_4^{pq} \frac{\partial u_0}{\partial x} + a_5^{pq} \frac{\partial^2 w_0}{\partial x^2} + a_6^{pq} \frac{\partial \psi}{\partial x} + \mu_2^{pq} \phi_0 + \beta_2^{pq} \frac{\partial \phi_0}{\partial x} \qquad (17b)$$

$$\hat{M}_{xx}^{pq} = a_7^{pq} \frac{\partial u_0}{\partial x} + a_8^{pq} \frac{\partial^2 w_0}{\partial x^2} + a_9^{pq} \frac{\partial \psi}{\partial x} + \mu_3^{pq} \phi_0 + \beta_3^{pq} \frac{\partial \phi_0}{\partial x} \qquad (17c)$$

$$\hat{Q}_{xz}^{pq} = a_{10}^{pq} \psi + a_{11}^{pq} \frac{\partial^2 \psi}{\partial x^2} + a_{12}^{pq} \frac{\partial^2 \psi}{\partial x^2} + a_{13}^{pq} \frac{\partial^3 w_0}{\partial x^3} + \mu_4^{pq} \phi_0 + \beta_4^{pq} \frac{\partial \phi_0}{\partial x} \qquad (17d)$$

where the coefficients a_i^{pq} $(i = 1, 2, \ldots, 13)$, β_i^{pq} $(i = 1, 2, \ldots, 4)$, and μ_i^{pq} $(i = 1, 2, \ldots, 4)$ are functions of the geometry parameters as well as mechanical and electrical properties of both FGP core and piezoelectric layers which are defined in relations (A.1-A.4) of the Appendix. It should be mentioned that these coefficients have different values for transverse and shear modes as well as SC and OC electrical boundary conditions, as reported in the Appendix.

Substituting Equations (17) into Equations (13a) to (13c) leads to the beam equations of motion in terms of displacement field components and the electric potential function:

$$a_1^{pq} \frac{\partial^2 u_0}{\partial x^2} + a_2^{pq} \frac{\partial^3 w_0}{\partial x^3} + a_3^{pq} \frac{\partial^2 \psi}{\partial x^2} + \mu_1^{pq} \frac{\partial \phi_0}{\partial x} + \beta_1^{pq} \frac{\partial^2 \phi_0}{\partial x^2} - I_0 \frac{\partial^2 u_0}{\partial t^2} - I_{01} \frac{\partial^2 \psi}{\partial t^2}$$
$$+ I_1 \frac{\partial^3 w_0}{\partial x \partial t^2} = 0 \tag{18a}$$

$$a_4^{pq} \frac{\partial^3 u_0}{\partial x^3} + a_5^{pq} \frac{\partial^4 w_0}{\partial x^4} + a_6^{pq} \frac{\partial^3 \psi}{\partial x^3} + \mu_2^{pq} \frac{\partial^2 \phi_0}{\partial x^2} + \beta_2^{pq} \frac{\partial^3 \phi_0}{\partial x^3} - I_1 \frac{\partial^3 u_0}{\partial x \partial t^2} - I_{11} \frac{\partial^3 \psi}{\partial x \partial t^2}$$
$$- I_0 \frac{\partial^2 w_0}{\partial t^2} + I_2 \frac{\partial^4 w_0}{\partial x^2 \partial t^2} = 0 \tag{18b}$$

$$\left(a_7^{pq} - a_{12}^{pq}\right) \frac{\partial^2 u_0}{\partial x^2} + \left(a_8^{pq} - a_{13}^{pq}\right) \frac{\partial^3 w_0}{\partial x^3} + \left(a_9^{pq} - a_{11}^{pq}\right) \frac{\partial^2 \psi}{\partial x^2} - a_{10}^{pq} \psi$$
$$+ \left(\mu_3^{pq} - \beta_4^{pq}\right) \frac{\partial \phi_0}{\partial x} + \beta_3^{pq} \frac{\partial^2 \phi_0}{\partial x^2} - \mu_4^{pq} \phi_0 - I_{01} \frac{\partial^2 u_0}{\partial t^2} - I_{02} \frac{\partial^2 \psi}{\partial t^2} \tag{18c}$$
$$+ I_{11} \frac{\partial^3 w_0}{\partial x \partial t^2} = 0$$

After deriving the above governing equations for the smart FGP beam, the last equation which is actually the electric displacement equation coupled with the induced mechanical displacements could be determined according to the Maxwell's approach:

$$\int_{-t_c - t_p}^{-t_c} \left(D_{x,x}^{pq} + D_{z,z}^{pq}\right) dz + \int_{+t_c}^{+t_c + t_p} \left(D_{x,x}^{pq} + D_{z,z}^{pq}\right) dz = 0 \tag{19}$$

Using Equations (4), (5) and (9), and substituting the electric displacement field components in the Equation (19), the last electromechanical governing equation can be derived for both transverse and shear modes as follows:

$$b_1^{pq} \psi + b_2^{pq} \frac{\partial \psi}{\partial x} + b_3^{pq} \frac{\partial^2 \psi}{\partial x^2} + b_4^{pq} \frac{\partial^3 \psi}{\partial x^3} + b_5^{pq} \frac{\partial^2 u_0}{\partial x^2} + b_6^{pq} \frac{\partial^3 u_0}{\partial x^3} + b_7^{pq} \frac{\partial^2 w_0}{\partial x^2} + b_8^{pq} \frac{\partial^3 w_0}{\partial x^3}$$
$$+ b_9^{pq} \frac{\partial^4 w_0}{\partial x^4} + \mu_5^{pq} \phi_0 + \beta_5^{pq} \frac{\partial^2 \phi_0}{\partial x^2} = 0 \tag{20}$$

The coefficients b_i^{pq} ($i = 1, \dots, 9$), μ_5^{pq} and β_5^{pq} are defined in relation (A.1-A.4) of the Appendix for all the considered piezoelectric modes and electrical boundary conditions.

5. Solution Procedure

In the previous section, all four electromechanical governing equations of motion (18a) to (18c) and (20) were derived according to the considered mechanical displacement field. Here, it is assumed that the edges $x=0$ and $x=L$ of the sandwich beam are mechanically simply supported and electrically grounded to zero potential in both transverse and shear modes. Therefore, the essential and natural BC's (16) can be expressed for beams with simply supported edges as follows:

$$N_{xx}^{pq} = w_0 = M_{xx}^{pq} = \widehat{M}_{xx}^{pq} = \phi_0 = 0 \tag{21}$$

The Navier-type procedure is employed to analytically solve the governing equations (18) and (20) to determine the exact natural frequencies, thus the unknown components of the mechanical displacement field as well as the electric potential function may be of the form:

$$\begin{Bmatrix} u_0 \\ \psi \\ w_0 \\ \phi_0 \end{Bmatrix} = \sum_{m=1}^{\infty} \begin{Bmatrix} X_m^{u_0} \cos(\beta_m x) \\ X_m^{\psi} \cos(\beta_m x) \\ X_m^{w_0} \sin(\beta_m x) \\ X_m^{\phi_0} \sin(\beta_m x) \end{Bmatrix} T(t) \qquad (22)$$

where m denotes number of half-waves in the axial direction and $\beta_m = m\pi/L$. Also, $X_m^{u_0}$, X_m^{ψ}, $X_m^{w_0}$ and $X_m^{\phi_0}$ are the unknown coefficients, and $T(t) = e^{i\omega t}$ in which $i = \sqrt{-1}$ and ω is the natural frequency of the system. It can be simply verified that the considered set of series for the unknowns can satisfy the obtained BC's stated in relation (21).

Substituting the expansions of u_0, ψ, w_0 and ϕ_0 from equations (22) into the governing equations (18) and (20) results in the following eigenvalue problem:

$$\left(\begin{bmatrix} k_{11} & k_{12} & k_{13} & k_{14} \\ k_{21} & k_{22} & k_{23} & k_{24} \\ k_{31} & k_{32} & k_{33} & k_{34} \\ k_{41} & k_{42} & k_{43} & k_{44} \end{bmatrix} - \omega^2 \begin{bmatrix} m_{11} & m_{12} & m_{13} & m_{14} \\ m_{21} & m_{22} & m_{23} & m_{24} \\ m_{31} & m_{32} & m_{33} & m_{34} \\ m_{41} & m_{42} & m_{43} & m_{44} \end{bmatrix} \right) \begin{Bmatrix} X_m^{u_0} \\ X_m^{\psi} \\ X_m^{w_0} \\ X_m^{\phi_0} \end{Bmatrix} = \begin{Bmatrix} 0 \\ 0 \\ 0 \\ 0 \end{Bmatrix} \qquad (23)$$

in which $[k]$, $[m]$ and $\{X\}$ denote the stiffness matrix, mass matrix and the vector of unknown coefficients, respectively. Equation (23) represents a system of four algebraic homogenous equations in terms of the unknown coefficients. For a nontrivial solution of the vector of coefficients $\{X\}$, the determinant of the coefficient matrix must be set to zero (i.e. $|[k] - \omega^2[m]| = 0$), which yields a characteristic equation in terms of ω. Positive real roots of this equation are the natural free vibration frequencies of the smart FGP beam.

6. Numerical Results and Discussion

6.1. Verification Studies

First, to ensure the accuracy of the present models and formulations, the obtained numerical results are compared with those available in the literature. It must be mentioned that due to slight variation of the Poisson ratio v through the thickness direction of the core layer, its value is assumed to be constant (equal to $v=0.3$)[44, 55]. In Table 2, for a sandwich beam composed of an isotropic core and d_{31} piezoelectric layers, the present results are compared with those reported by Pradhan et al.[9]. It is obvious that as the value of $t_p/2t_c$ goes to zero, the natural frequencies of the sandwich beam approach those of the homogenous beam. The numerical results reported by Pradhan et al.[9] are calculated based on Bernoulli-Euler's and Timoshenko's beam theories (called CBT and TBT, respectively, in the study of Pradhan et al.[9]) using Rayleigh-Ritz's approach, for the following material properties of an FGM beam:

Alumina: $E_c=380$ GPa, $\rho_c=3800$ kg/m³, $v_c=0.3$

Aluminum: E_m=70 GPa, ρ_m=2700 kg/m^3, ν_m=0.3

Table 2. Comparison of the first five dimensionless frequencies, $[\omega L^2/2t_c]\sqrt{\rho_m/E_m}$, with those reported in the studies of Pradhan et al.[9] ($\alpha = 0, k = 0$)

$t_p/2t_c$	Reference	1st mode	2nd mode	3rd mode	4th mode	5th mode
$L/2t_c = 20$						
10^{-1}	CBT (Present)	6.1549	24.4738	54.5326	95.6643	126.7363
10^{-2}	CBT (Present)	6.8282	27.2202	60.9025	107.4347	149.8236
10^{-3}	CBT (Present)	6.9386	27.6686	61.9359	109.3302	153.0845
10^{-4}	CBT (Present)	6.9503	27.7160	62.0450	109.5302	153.4245
10^{-5}	CBT (Present)	6.9515	27.7207	62.0560	109.5503	153.4586
0	CBT (Present)	6.9516	27.7212	62.0572	109.5525	153.4624
0	CBT (Pradhan et al.[9])	6.9516	27.7212	62.0573	109.5542	153.4624
$L/2t_c = 5$						
10^{-1}	CBT (Present)	5.9790	22.0144	31.6841	44.2232	63.3681
10^{-2}	CBT (Present)	6.7147	25.5444	37.4559	53.3843	74.9118
10^{-3}	CBT (Present)	6.8331	26.1012	38.2711	54.8405	76.5422
10^{-4}	CBT (Present)	6.8456	26.1599	38.3561	54.9946	76.7122
10^{-5}	CBT (Present)	6.8469	26.1658	38.3646	55.0102	76.7293
0	CBT (Present)	6.8470	26.1665	38.3656	55.0119	76.7312
0	CBT (Pradhan et al.[9])	6.8470	26.1665	38.3655	55.0119	76.7312

In Table 3, the fundamental frequency of a simply supported beam made of FGMs is computed for different power-law indices namely 0, 0.5, 1, 2, 5 and 10 and compared with those of Pradhan et al.[9] and Metin et al.[56]. As one can see from Table 2 and the second column of Table 3, when $k = 0$, the present results correspond closely to those of Metin et al.[56] and Pradhan et al.[9] which were computed based on analytical and numerical (i.e. Rayleigh-Ritz) methods, respectively. For $k \neq 0$, again, excellent agreement is clearly seen when compared with the analytically computed results of Metin et al.[56]. However, in some cases, the differences between the results of the present analytical models and the Rayleigh-Ritz's method which was used in the study of Pradhan et al.[9] are greater compared to those with the frequency values predicted by Metin et al[56]. It is possible that the numerical approach used in the work of Pradhan et al.[9] did not give fully converged values of the frequencies.

Table 3. Comparison of the dimensionless fundamental frequency, $[\omega L^2/2t_c]\sqrt{\rho_m/E_m}$, of a FG beam with those of Pradhan et al.[9] and Metin et al.[56] for different values of power-law index ($L/2t_c = 20, \alpha = 0$)

Theory	k=0	k=0.5	k=1	k=2	k=5	k=10
CBT (Pradhan et al.[9])	6.9516	5.7627	5.2563	4.8259	4.3803	4.0208
CBT (Metin et al.[56])	6.9510	-	4.9070	4.3340	-	3.8040
CBT (Present)	6.9516	5.5942	4.9039	4.3305	3.9814	3.7998
FBT (Pradhan et al.[9])	6.9317	5.7471	5.2417	4.8112	4.3647	4.0059
FBT (Metin et al.[56])	6.9310	-	4.8950	4.3230	-	3.7910
FBT (Present)	6.9314	5.5797	4.8919	4.3197	3.9695	3.7870
PBT (Present)	6.9273	5.5770	4.8895	4.3168	3.9643	3.7815
SBT (Present)	6.9274	5.5771	4.8895	4.3168	3.9641	3.7814
EBT (Present)	6.9275	5.5771	4.8895	4.3168	3.9641	3.7814

To further asses the calculated results by the present models, the fundamental resonant frequencies of an FG beam with $k = 1$ are calculated and the dimensionless results are listed in Table 4 for three values of $L/2t_c$ alongside those of Su et al.[57] in which the Bernoulli-Euler's beam theory in conjunction with the Wittrick-Williams's algorithm are used to extract the natural frequencies. A maximum error of 3% is seen among the results, which may be appeared due to employing the different numerical and analytical solution approaches developed in the two studies.

Table 4. Comparison of the dimensionless fundamental frequency of a FG beam, $[100\omega(2t_c)]\sqrt{\rho_m/E_m}$, with those of Su et al.[57] for different values of $L/2t_c$ ($k = 1, \alpha = 0$)

Theory	$L/2t_c = 5$	$L/2t_c = 10$	$L/2t_c = 100$
CBT (Su et al.[57])	15.436	3.9059	0.039218
CBT (Present)	15.912	4.0312	0.040492
FBT (Present)	15.275	3.9868	0.040487
PBT (Present)	15.157	3.9781	0.040486
SBT (Present)	15.158	3.9782	0.040486
EBT (Present)	15.162	3.9784	0.040486

Having completed the above verification examples that confirmed the accuracy of the present model, a parametric study covering the effects of various significant beam parameters and piezoelectric characteristics on the system's response is now performed.

6.2. New results and simulations

In this section, new results are presented in both tabular and graphical forms for the free vibration of FGP beams integrated with d_{31} and d_{15} piezoelectric layers. The mechanical and electrical properties of the materials used in this study are listed in Table 5[58]. Al and Al_2O_3 are considered as the metal and ceramic parts of the FGM core, respectively; and the piezoelectric layers are assumed to be made of PZT-5H.

Table 5. Mechanical and electrical properties of materials[58]

Material	Properties							
	Elastic moduli (*GPa*)						Dielectric moduli (10^{-9} *F/m*)	
	C_{11}	C_{12}	C_{33}	C_{13}	C_{55}	C_{66}	Ξ_{11}	Ξ_{33}
PZT-2	134.9	67.9	113.3	68.1	22.2	33.4	4.46	2.4
PZT-4	139.0	77.8	115.0	74.3	25.6	30.6	6.75	5.9
PZT-5H	127.2	80.2	117.4	84.7	23.0	23.5	15.1	12.7
	Piezoelectric moduli (*C/m²*)				Density (*kg/m³*)		Young's modulus (*GPa*)	
	e_{31}	e_{33}	e_{15}		ρ		E	
PZT-2	-1.82	9.05	9.8		7600		-	
PZT-4	-5.2	15.1	12.7		7500		-	
PZT-5H	-6.6	23.2	17.0		7500		-	
Aluminum (Al)	-	-	-		2700		70	
Alumina (Al_2O_3)	-	-	-		3800		380	

In Tables 6 to 9, based on the presented CBT, FBT, PBT, SBT and EBT, the effects of porosity volume fraction α, porosity distribution, power-law index k and electrical circuit condition on the

resonance frequencies of both d_{31} and d_{15} piezoelectric coupled FGP beams are investigated. These tables list the first three SC and OC eigenfrequencies of smart FGP beams for different values of power-law index and porosity parameter.

These tables imply that FGP beams sandwiched between d_{15} piezoelectric layers provide lower SC and OC resonant frequencies in comparison with the ones corresponding to the beams surrounded by d_{31} piezoelectric layers. In addition, when the bonded piezoelectric layers are polarized through their thickness, the OC natural frequencies are considerably larger than those of the similar beams with SC electrical condition, whereas there is almost no difference between SC and OC resonant frequencies when the beams are surrounded by d_{15} piezoelectric layers. Moreover, the power-law index plays an important role on the frequency behavior of the smart FGP beams. As seen in the tables, for both even and uneven porosity distributions, increasing the power-law index significantly decreases the first three natural frequencies of the smart sandwich beam irrespective of the value of α, piezoelectricity mode and electrical boundary condition. This is due to the fact that an increase in the value of k leads to a decrease in the effective modulus of elasticity, and consequently the beam becomes less rigid. Thus, as it is well-known from mechanical vibration, resonance frequencies reduce as the structure stiffness decreases. Considering the tabulated results in Tables 6 to 9, it is obvious that the beam resonant frequencies are the same for both even and uneven porosity distribution, when $\alpha=0$. This is due to the considered functions for the mechanical properties of FGMs with porosity which are defined by Equation (1). For the studied power-law indices and porosity parameters, the smart FGP beams with uneven porosity pattern exhibit higher frequencies than those of the beams with evenly distributed pores. Inspection of these tables reveals that the natural frequencies predicted by CBT are comparatively greater than those forecasted by higher deformation beam theories, regardless of the considered electrical and material parameters of the smart FGP beams. It is also observed that the results of the higher-order theories (i.e. PBT, SBT and EBT) are close to each other for all the considered beam parameters.

Table 6. First three SC resonance frequencies (Hz) of piezoelectric coupled FGP beams with Even porosity distribution ($L/2t_c$=10, $t_p/2t_c$=0.2)

Source	Mode 1 (m=1)			Mode 2 (m=2)			Mode 3 (m=3)		
	K=0	K=1	K=10	K=0	K=1	K=10	K=0	K=1	K=10
α=0									
FGP Beam with d_{31} Piezoelectric Layers									
CBT	435.309	374.916	349.683	1691.218	1453.180	1353.334	3637.466	3114.708	2894.397
FBT	428.399	368.360	339.793	1600.435	1368.370	1230.287	3286.992	2793.157	2444.241
PBT	427.996	368.151	337.747	1594.783	1365.460	1207.247	3263.123	2781.008	2367.621
SBT	427.979	368.172	337.624	1594.517	1365.688	1205.928	3261.883	2781.719	2363.508
EBT	427.974	368.205	337.529	1594.398	1366.072	1204.915	3261.190	2783.005	2360.444
FGP Beam with d_{15} Piezoelectric Layers									
CBT	429.433	367.290	340.917	1668.391	1423.583	1319.352	3588.370	3051.166	2821.552
FBT	422.792	361.115	331.726	1581.021	1343.545	1204.554	3250.641	2747.146	2400.152
PBT	422.360	360.873	329.753	1574.984	1340.207	1182.130	3225.237	2733.332	2324.884
SBT	422.339	360.888	329.631	1574.662	1340.358	1180.794	3223.773	2733.751	2320.650
EBT	422.329	360.914	329.533	1574.480	1340.656	1179.743	3222.836	2734.716	2317.404
α=0.15									
FGP Beam with d_{31} Piezoelectric Layers									
CBT	438.306	371.104	343.240	1700.688	1435.809	1325.258	3651.151	3069.517	2824.439
FBT	431.172	364.338	331.531	1607.609	1349.187	1183.332	3294.759	2744.973	2318.360
PBT	430.770	364.163	327.491	1602.029	1346.743	1140.739	3271.113	2734.810	2184.861
SBT	430.763	364.196	327.167	1601.815	1347.125	1137.516	3270.049	2736.085	2175.412
EBT	430.763	364.243	326.872	1601.754	1347.675	1134.621	3269.554	2737.970	2167.085
FGP Beam with d_{15} Piezoelectric Layers									
CBT	432.023	362.684	333.362	1676.310	1403.179	1286.971	3598.814	2999.601	2742.457
FBT	425.183	356.356	322.589	1586.941	1321.977	1155.814	3256.171	2694.766	2272.850
PBT	424.756	356.147	318.791	1580.953	1319.103	1115.291	3230.911	2682.946	2144.459
SBT	424.739	356.174	318.483	1580.677	1319.398	1112.175	3229.607	2683.899	2135.195
EBT	424.733	356.213	318.201	1580.548	1319.851	1109.361	3228.849	2685.428	2126.979
α=0.3									
FGP Beam with d_{31} Piezoelectric Layers									
CBT	441.771	365.741	333.189	1711.595	1411.897	1281.583	3666.819	3008.766	2715.761
FBT	434.368	358.731	317.771	1615.777	1323.272	1103.598	3303.404	2681.509	2108.475
PBT	433.977	358.594	303.600	1610.253	1321.386	975.9310	3279.916	2673.802	1755.067
SBT	433.970	358.644	301.470	1610.100	1321.975	959.1190	3279.057	2675.826	1713.398
EBT	433.976	358.710	299.089	1610.108	1322.746	940.9700	3278.793	2678.506	1669.579
FGP Beam with d_{15} Piezoelectric Layers									
CBT	435.020	356.298	321.571	1685.438	1375.361	1236.523	3610.783	2930.664	2619.086
FBT	427.942	349.803	307.633	1593.686	1293.026	1074.488	3262.293	2625.992	2063.365
PBT	427.518	349.634	294.665	1587.728	1290.733	955.2960	3237.110	2616.738	1728.135
SBT	427.506	349.676	292.705	1587.508	1291.223	939.4290	3235.992	2618.404	1688.057
EBT	427.505	349.732	290.511	1587.441	1291.883	922.2590	3235.443	2620.684	1645.799

Table 7. First three OC resonance frequencies (Hz) of piezoelectric coupled FGP beams with Even porosity distribution ($L/2t_c$=10, $t_p/2t_c$=0.2)

Source	Mode 1 (m=1)			Mode 2 (m=2)			Mode 3 (m=3)		
	K=0	K=1	K=10	K=0	K=1	K=10	K=0	K=1	K=10
α=0									
FGP Beam with d_{31} Piezoelectric Layers									
CBT	437.319	377.513	352.659	1699.004	1463.229	1364.830	3654.124	3136.178	2918.911
FBT	430.260	370.747	342.382	1606.324	1375.787	1237.283	3296.560	2804.957	2453.361
PBT	429.908	370.606	340.405	1601.322	1373.728	1215.129	3275.147	2795.954	2379.920
SBT	429.895	370.631	340.288	1601.100	1374.015	1213.873	3274.074	2796.888	2376.040
EBT	429.893	370.669	340.198	1601.024	1374.460	1212.928	3273.551	2798.402	2373.227
FGP Beam with d_{15} Piezoelectric Layers									
CBT	429.433	367.290	340.917	1668.391	1423.595	1319.362	3588.370	3051.225	2821.608
FBT	423.017	361.454	332.786	1583.783	1347.653	1216.734	3260.564	2761.687	2441.427
PBT	422.360	360.874	329.753	1574.984	1340.216	1182.137	3225.237	2733.371	2324.910
SBT	422.339	360.889	329.631	1574.662	1340.367	1180.801	3223.773	2733.790	2320.676
EBT	422.329	360.915	329.534	1574.480	1340.665	1179.750	3222.836	2734.754	2317.429
α=0.15									
FGP Beam with d_{31} Piezoelectric Layers									
CBT	440.454	373.966	346.592	1708.998	1446.871	1338.171	3668.898	3093.103	2851.946
FBT	433.157	366.960	334.357	1613.855	1357.261	1190.439	3304.845	2757.701	2326.738
PBT	432.816	366.860	330.351	1608.978	1355.760	1148.459	3283.841	2750.981	2195.712
SBT	432.807	366.899	330.029	1608.812	1356.210	1145.272	3282.957	2752.506	2186.432
EBT	432.811	366.952	329.736	1608.799	1356.829	1142.420	3282.646	2754.647	2178.294
FGP Beam with d_{15} Piezoelectric Layers									
CBT	432.023	362.685	333.363	1676.310	1403.195	1286.991	3598.814	2999.686	2742.571
FBT	425.437	356.759	324.260	1590.035	1326.799	1174.401	3267.203	2711.650	2334.091
PBT	424.756	356.148	318.792	1580.953	1319.116	1115.303	3230.911	2683.001	2144.497
SBT	424.739	356.175	318.484	1580.677	1319.411	1112.186	3229.607	2683.954	2135.233
EBT	424.733	356.214	318.202	1580.548	1319.864	1109.372	3228.849	2685.482	2127.015
α=0.3									
FGP Beam with d_{31} Piezoelectric Layers									
CBT	444.079	368.944	337.096	1720.506	1424.256	1296.685	3685.808	3035.060	2748.004
FBT	436.494	361.651	320.876	1622.424	1332.172	1110.363	3314.058	2695.388	2114.974
PBT	436.164	361.600	306.425	1617.666	1331.338	981.4270	3293.427	2691.468	1760.467
SBT	436.161	361.657	304.244	1617.565	1332.004	964.3930	3292.765	2693.774	1718.554
EBT	436.171	361.729	301.807	1617.626	1332.855	946.0130	3292.702	2696.744	1674.495
FGP Beam with d_{15} Piezoelectric Layers									
CBT	435.020	356.300	321.574	1685.438	1375.385	1236.574	3610.783	2930.793	2619.379
FBT	428.232	350.292	310.864	1597.194	1298.812	1108.407	3274.695	2646.008	2169.794
PBT	427.518	349.635	294.668	1587.728	1290.753	955.3130	3237.110	2616.820	1728.172
SBT	427.506	349.677	292.707	1587.508	1291.243	939.4440	3235.992	2618.485	1688.087
EBT	427.505	349.734	290.513	1587.441	1291.902	922.2730	3235.443	2620.765	1645.823

Table 8. First three SC resonance frequencies (Hz) of piezoelectric coupled FGP beams with Uneven porosity distribution ($L/2t_c$=10, $t_p/2t_c$=0.2)

Source	Mode 1 (m=1)			Mode 2 (m=2)			Mode 3 (m=3)		
	K=0	K=1	K=10	K=0	K=1	K=10	K=0	K=1	K=10
α=0									
FGP Beam with d_{31} Piezoelectric Layers									
CBT	435.309	374.916	349.683	1691.218	1453.180	1353.334	3637.466	3114.708	2894.397
FBT	428.399	368.360	339.793	1600.435	1368.370	1230.287	3286.992	2793.157	2444.241
PBT	427.996	368.151	337.747	1594.783	1365.460	1207.247	3263.123	2781.008	2367.621
SBT	427.979	368.172	337.624	1594.517	1365.688	1205.928	3261.883	2781.719	2363.508
EBT	427.974	368.205	337.529	1594.398	1366.072	1204.915	3261.190	2783.005	2360.444
FGP Beam with d_{15} Piezoelectric Layers									
CBT	429.433	367.290	340.917	1668.391	1423.583	1319.352	3588.370	3051.166	2821.552
FBT	422.792	361.115	331.726	1581.021	1343.545	1204.554	3250.641	2747.146	2400.152
PBT	422.360	360.873	329.753	1574.984	1340.207	1182.130	3225.237	2733.332	2324.884
SBT	422.339	360.888	329.631	1574.662	1340.358	1180.794	3223.773	2733.751	2320.650
EBT	422.329	360.914	329.533	1574.480	1340.656	1179.743	3222.836	2734.716	2317.404
α=0.15									
FGP Beam with d_{31} Piezoelectric Layers									
CBT	439.971	377.265	351.524	1707.924	1460.703	1358.639	3669.067	3125.971	2900.099
FBT	432.801	370.392	340.421	1614.195	1372.408	1222.581	3309.303	2793.832	2409.524
PBT	432.322	370.068	336.877	1607.598	1368.134	1184.239	3281.976	2776.951	2286.552
SBT	432.297	370.078	336.543	1607.223	1368.227	1180.804	3280.334	2777.185	2276.160
EBT	432.283	370.101	336.225	1606.996	1368.482	1177.559	3279.244	2778.010	2266.487
FGP Beam with d_{15} Piezoelectric Layers									
CBT	433.944	369.355	342.375	1684.530	1430.031	1323.200	3618.811	3060.202	2824.199
FBT	427.057	362.893	332.084	1594.373	1346.847	1196.535	3272.307	2746.697	2365.818
PBT	426.551	362.542	328.713	1587.402	1342.203	1159.683	3243.480	2728.344	2246.465
SBT	426.521	362.546	328.393	1586.971	1342.223	1156.340	3241.617	2728.300	2236.224
EBT	426.502	362.562	328.085	1586.682	1342.395	1153.169	3240.285	2728.814	2226.649
α=0.3									
FGP Beam with d_{31} Piezoelectric Layers									
CBT	444.932	379.650	353.235	1725.657	1468.187	1363.125	3702.488	3136.641	2903.019
FBT	437.477	372.417	340.506	1628.719	1375.999	1210.070	3332.682	2792.822	2360.871
PBT	436.907	371.940	333.870	1621.001	1369.924	1142.228	3301.309	2769.798	2153.628
SBT	436.871	371.934	332.968	1620.492	1369.823	1133.638	3299.182	2769.363	2129.197
EBT	436.846	371.940	331.997	1620.133	1369.885	1124.572	3297.609	2769.523	2103.865
FGP Beam with d_{15} Piezoelectric Layers									
CBT	438.746	371.426	343.640	1701.665	1436.329	1325.973	3651.012	3068.418	2823.493
FBT	431.589	364.641	331.878	1608.471	1349.642	1183.837	3295.021	2744.491	2318.004
PBT	430.993	364.144	325.630	1600.396	1343.283	1119.174	3262.199	2720.277	2118.325
SBT	430.952	364.132	324.777	1599.832	1343.116	1110.937	3259.855	2719.587	2094.601
EBT	430.923	364.133	323.859	1599.412	1343.102	1102.234	3258.042	2719.457	2069.968

Table 9. First three OC resonance frequencies (Hz) of piezoelectric coupled FGP beams with Uneven porosity distribution ($L/2t_c$=10, $t_p/2t_c$=0.2)

Source	Mode 1 (m=1)			Mode 2 (m=2)			Mode 3 (m=3)		
	K=0	K=1	K=10	K=0	K=1	K=10	K=0	K=1	K=10
α=0									
FGP Beam with d_{31} Piezoelectric Layers									
CBT	437.319	377.513	352.659	1699.004	1463.229	1364.830	3654.124	3136.178	2918.911
FBT	430.260	370.747	342.382	1606.324	1375.787	1237.283	3296.560	2804.957	2453.361
PBT	429.908	370.606	340.405	1601.322	1373.728	1215.129	3275.147	2795.950	2379.920
SBT	429.895	370.631	340.288	1601.100	1374.015	1213.873	3274.074	2796.888	2376.040
EBT	429.893	370.669	340.198	1601.024	1374.460	1212.928	3273.551	2798.402	2373.227
FGP Beam with d_{15} Piezoelectric Layers									
CBT	429.433	367.290	340.917	1668.391	1423.595	1319.362	3588.370	3051.225	2821.608
FBT	423.017	361.454	332.786	1583.783	1347.653	1216.734	3260.564	2761.687	2441.427
PBT	422.360	360.874	329.753	1574.984	1340.216	1182.137	3225.237	2733.371	2324.910
SBT	422.339	360.889	329.631	1574.662	1340.367	1180.801	3223.773	2733.790	2320.676
EBT	422.329	360.915	329.534	1574.480	1340.665	1179.750	3222.836	2734.754	2317.429
α=0.15									
FGP Beam with d_{31} Piezoelectric Layers									
CBT	442.033	379.958	354.626	1715.902	1471.113	1370.618	3686.116	3148.183	2925.620
FBT	434.706	372.857	343.076	1620.188	1380.001	1229.467	3318.972	2805.783	2417.995
PBT	434.279	372.604	339.576	1614.259	1376.601	1191.799	3294.162	2792.113	2297.641
SBT	434.257	372.619	339.244	1613.928	1376.755	1188.396	3292.690	2792.573	2287.402
EBT	434.247	372.646	338.927	1613.747	1377.071	1185.187	3291.774	2793.629	2277.899
FGP Beam with d_{15} Piezoelectric Layers									
CBT	433.944	369.356	342.376	1684.530	1430.045	1323.214	3618.811	3060.272	2824.277
FBT	427.302	363.277	333.452	1597.366	1351.455	1211.953	3283.004	2762.890	2417.196
PBT	426.551	362.543	328.714	1587.402	1342.214	1159.691	3243.480	2728.380	2246.495
SBT	426.521	362.547	328.393	1586.971	1342.234	1156.348	3241.617	2728.344	2236.253
EBT	426.502	362.563	328.086	`1586.682`	`1342.405`	`1153.177`	`3240.285`	`2728.858`	`2226.677`
α=0.3									
FGP Beam with d_{31} Piezoelectric Layers									
CBT	447.048	382.448	356.485	1733.838	1478.994	1375.669	3719.949	3159.672	2929.730
FBT	439.427	374.969	343.226	1634.818	1383.778	1216.747	3342.450	2804.919	2368.464
PBT	438.911	374.564	336.568	1627.787	1378.595	1149.089	3313.654	2785.155	2162.713
SBT	438.879	374.562	335.654	1627.323	1378.554	1140.446	3311.700	2784.945	2138.260
EBT	438.858	374.574	334.672	1627.010	1378.679	1131.324	3310.303	2785.337	2112.907
FGP Beam with d_{15} Piezoelectric Layers									
CBT	438.746	371.427	343.641	1701.665	1436.345	1325.993	3651.012	3068.502	2823.606
FBT	431.857	365.078	333.713	1611.727	1354.849	1204.022	3306.591	2762.647	2383.878
PBT	430.993	364.145	325.631	1600.396	1343.296	1119.185	3262.199	2720.329	2118.356
SBT	430.952	364.133	324.778	1599.832	1343.128	1110.947	3259.855	2719.639	2094.631
EBT	430.923	364.133	323.860	1599.412	1343.115	1102.243	3258.042	2719.509	2069.995

(a) Even	(b) Uneven
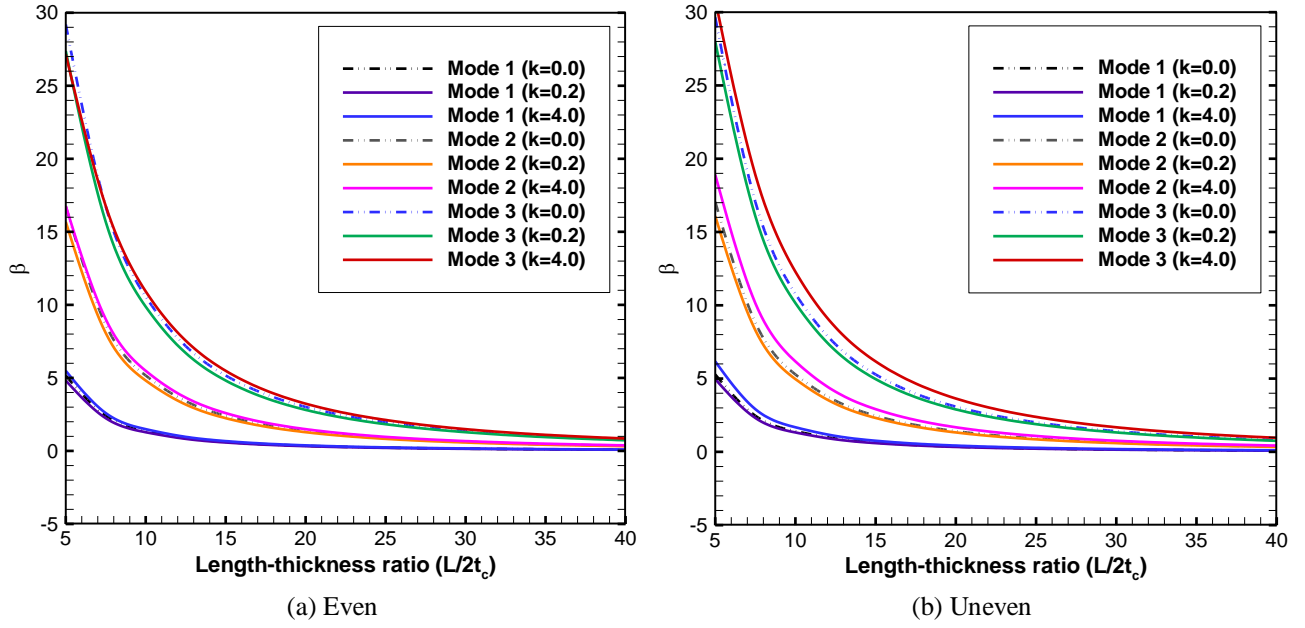
To gain a deeper insight into the effect of various beam theories on the eigenfrequency response, the variation β of percentage difference in frequency, defined by Equation (24), with respect to the length-thickness ratio $L/2t_c$ is plotted in Figure 3 for a FGP core beam with different patterns of porosity distribution.

$$\beta = \frac{\omega|_{\text{Predicted by CBT}} - \omega|_{\text{Predicted by PBT}}}{\omega|_{\text{Predicted by PBT}}} \times 100 \tag{24}$$

Since the frequencies predicted by higher-order beam theories are very close to each other, PBT is only employed in Equation (24). Figures (3a) and (3b) show the variation of β for the first three natural frequencies of FGP beams with different values of power-law index, namely 0, 0.2 and 4. As expected, positive values are obtained for β in all the vibration modes, which show that CBT predicts higher frequencies with respect to those calculated by PBT. As obvious in the figures, at a fixed value of $L/2t_c$, the amplitude of β is the most for the frequency related to the third vibrational mode, and the least value of β is determined for the fundamental frequency of the FGP beam. It does mean that there is a considerable difference between the results of CBT and higher-order theories, when calculating the frequencies of higher vibrational modes, especially for thicker beams (i.e. $L/2t_c < 15$). In other words, the influence of shear transverse deformation becomes more significant for thick beams and affects the corresponded results remarkably. Similar trends have been seen for FGP beams surrounded by surface-bonded piezoelectric layers. Hereafter, in order to increase the accuracy of the presented numerical simulations, all the figures are plotted based on the results of PBT, which virtually predicts the same frequencies as other higher-order theories presented in this study (i.e. SBT and EBT).

(a) Even - d_{31} Piezo Layers

(b) Uneven - d_{31} Piezo Layers

(c) Even - d_{15} Piezo Layers

(d) Uneven - d_{15} Piezo Layers
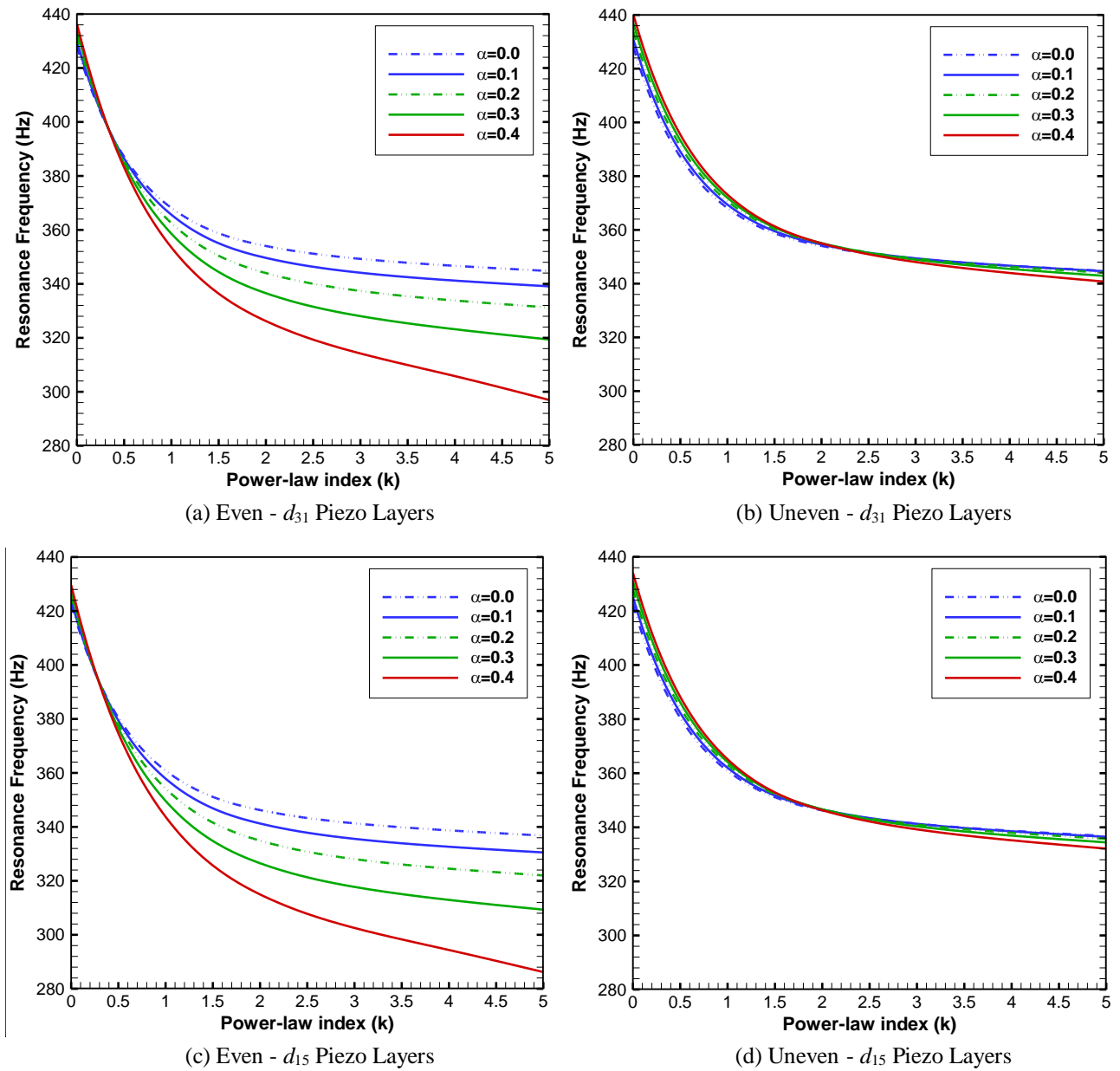
Figure 4. Variation of the fundamental natural frequency versus the power-law index for FGP beam with integrated piezoelectric layers in SC electrical condition ($L/2t_c$=10, $t_p/2t_c$=0.2)

One may see a specific upward or downward trend in Tables 6 to 9 for the eigenfrequency behavior of the smart FGP beams versus the porosity volume fraction for any given k regardless of the pattern of porosity distribution. For example, by carrying out a careful inspection of Tables 6 to 9, it can be ascertained that for k=0, the first three SC and OC natural frequencies increase as the value of α increases for both porosity distribution, whereas opposite trend is seen for frequencies of the beams with evenly distributed pores when the power-law index increases up to 1. To further investigate this matter, the effects of changes in the value of porosity parameter and the type of porosity distribution on variation of the SC fundamental frequency versus the power-law index are shown in Figure 4 for FGP beams with d_{31} and d_{15} piezoelectric layers. It can be observed that the free vibration behavior of the beam with even porosity distribution is influenced remarkably by changing the power-law index as well as the porosity parameter in comparison with the beam with uneven porosity distribution. Furthermore, it can be inferred from the figures that before the crossing point, the natural frequency increases as the value of α rises, while the opposite trend is seen after the mentioned point, regardless of the porosity distribution pattern and the type of piezoelectric layers. Moreover, the value

of k at the point of intersection is much higher for the hybrid FGP beam with unevenly distributed pores (around k=2.5) than that of the beam with even distribution (about k=0.3). Therefore, the trends for variation of the resonance frequencies versus porosity volume fraction depend on the value of power-law index for the beams with both even and uneven distribution.

Figures 5(a) to 5(f) show the combined effects of changes in power-law index and porosity distribution on variation of the first three eigenfrequencies of smart FGP beams with respect to the porosity volume fraction. Inspection of the figures concludes that the curves corresponded to even porosity distribution tend to incrementally lie below those related to beam with unevenly distributed pores, as k increases. Besides, for the small values of k, by increasing the porosity parameter, the SC and OC resonant frequencies of the first three vibrational modes increase, for both even and uneven porosity distribution. Nevertheless, the frequencies become lower as k is increased up to a prescribed value for FGP beams with even porosity distribution. This behavior can finally be seen for beams with unevenly distributed pores as the power-law index gets greater. These trends are seen mainly because the influence of dropping effective stiffness of the smart hybrid beam (owing to increasing k) overcomes its decreasing inertia at this point, which results in a downward trend for resonance frequencies. Similar trends may be observed for the FGP beams with d_{15} piezoelectric layers.
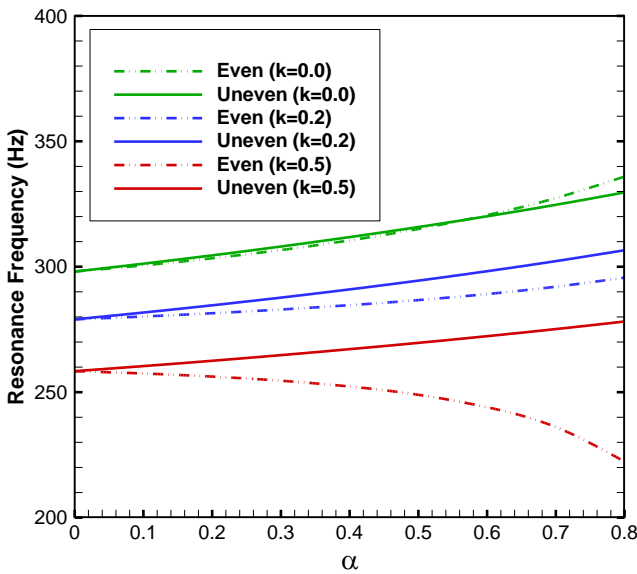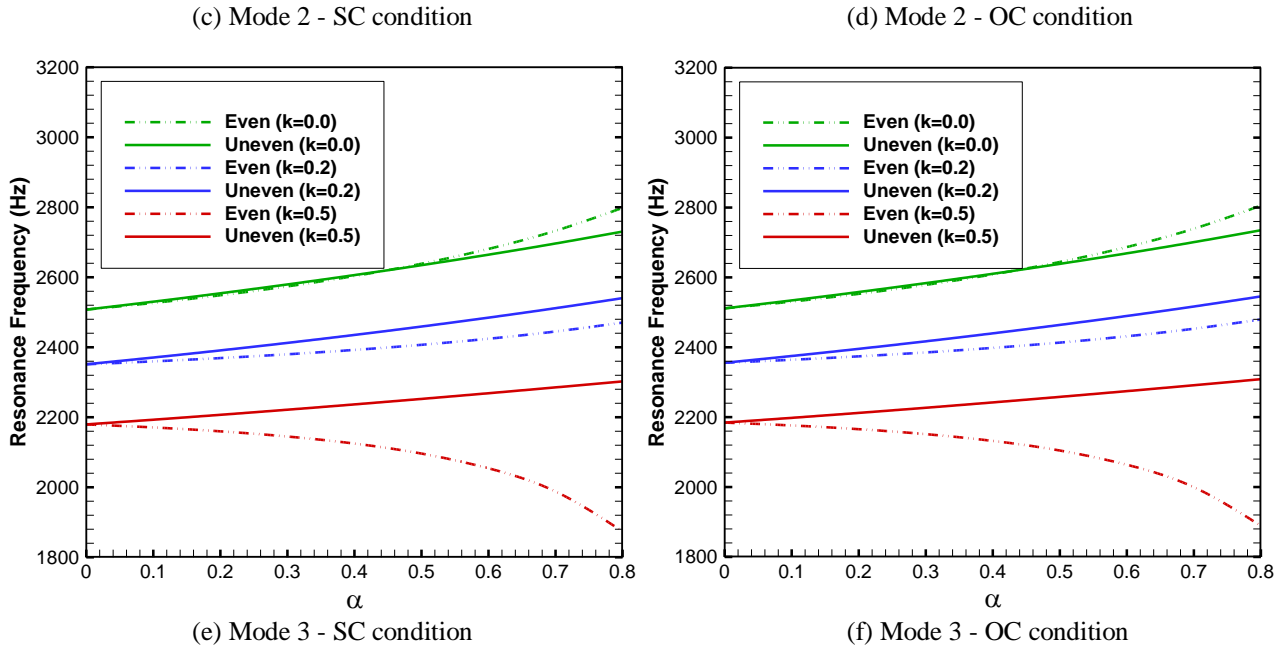

(a) Mode 1 - SC condition

(b) Mode 1 - OC condition

(c) Mode 2 - SC condition   (d) Mode 2 - OC condition
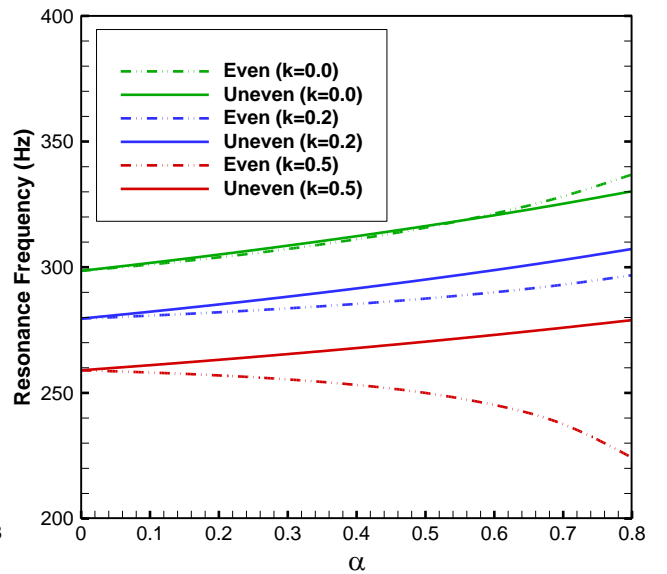
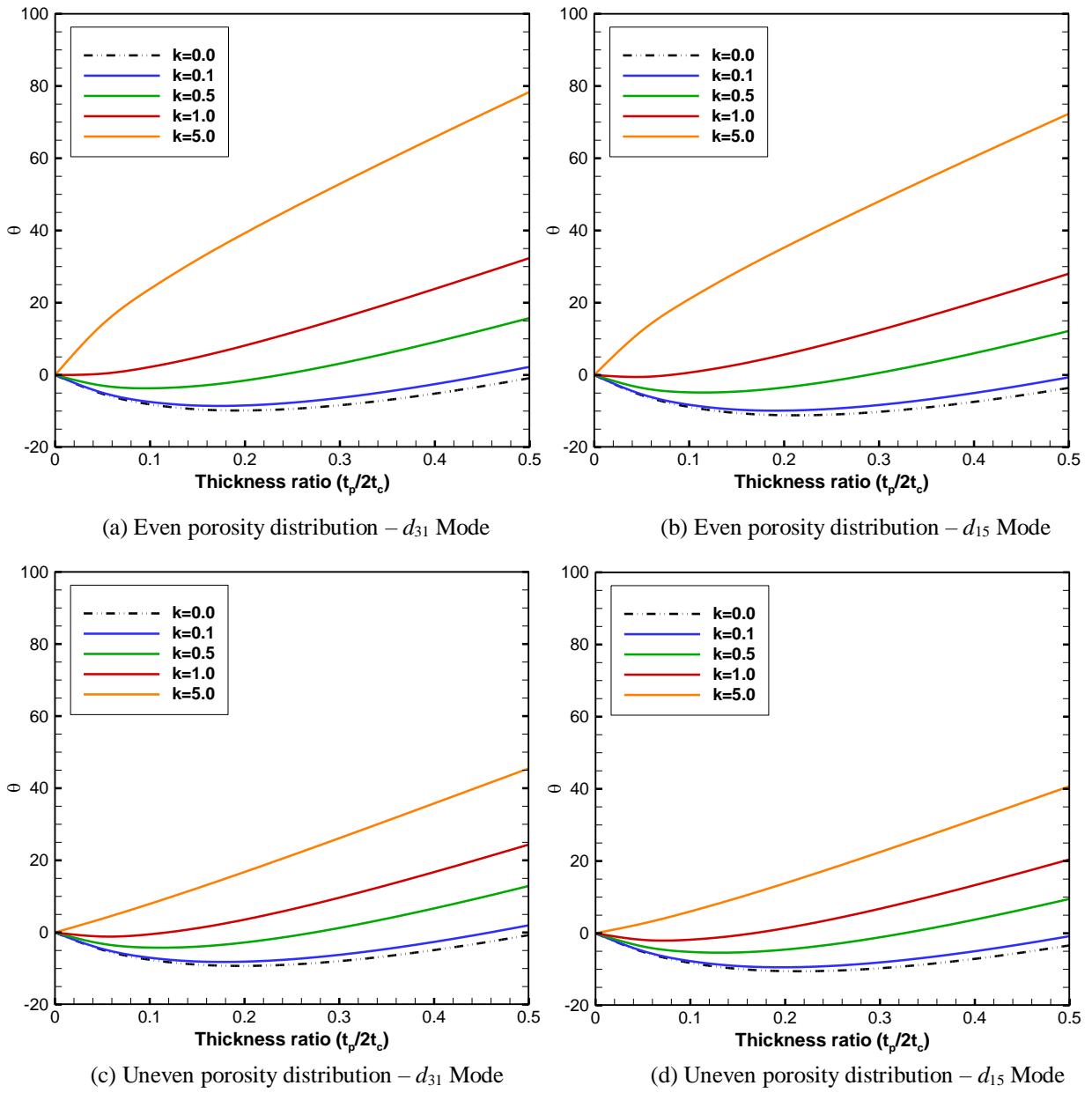(e) Mode 3 - SC condition   (f) Mode 3 - OC condition
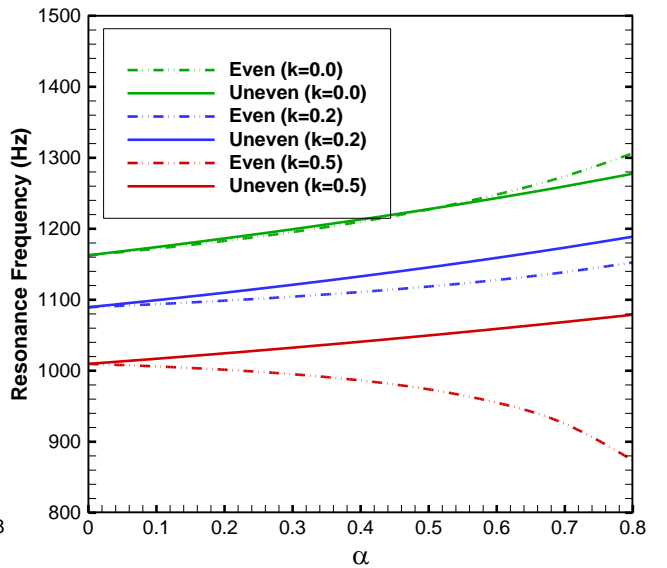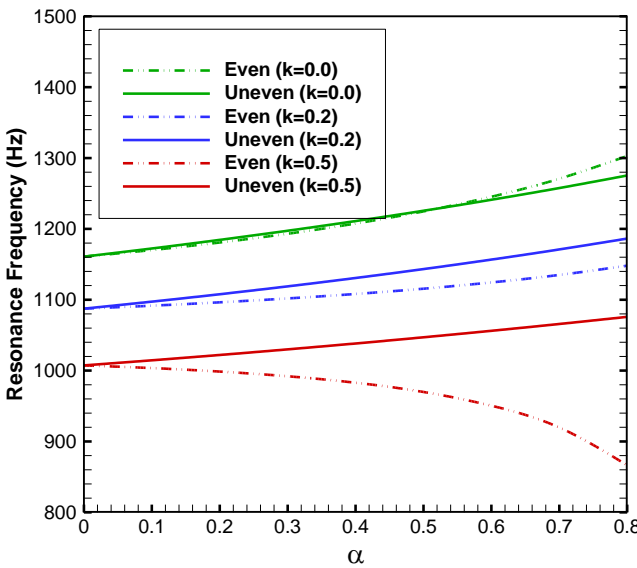
Figure 5. Variation of the first three SC and OC eigenfrequencies versus porosity volume fraction for FGP beam surrounded by d_{31} piezoelectric layers ($L/2t_c$=15, $2t_c/t_p$=15)
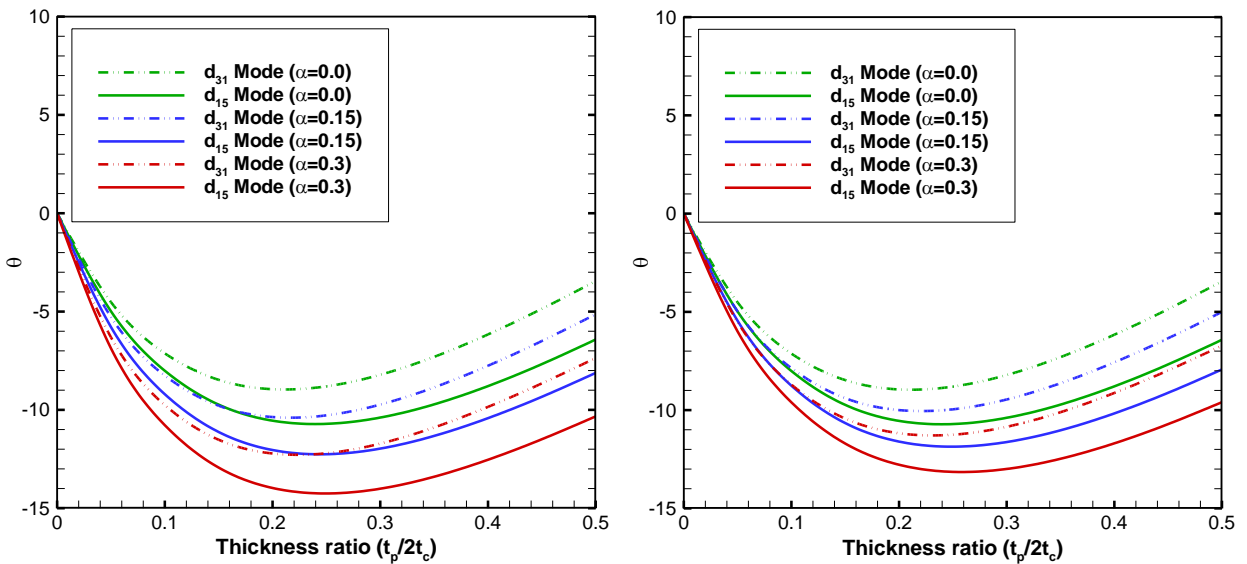
In the following, the influence of the piezoelectric layer thickness on the resonant frequencies of FGP beams are quantified for different power-law indices and porosity volume fractions. To this end, the new parameter θ, which represents the relative difference in natural frequency of the beams with and without piezoelectric layers is defined as follows
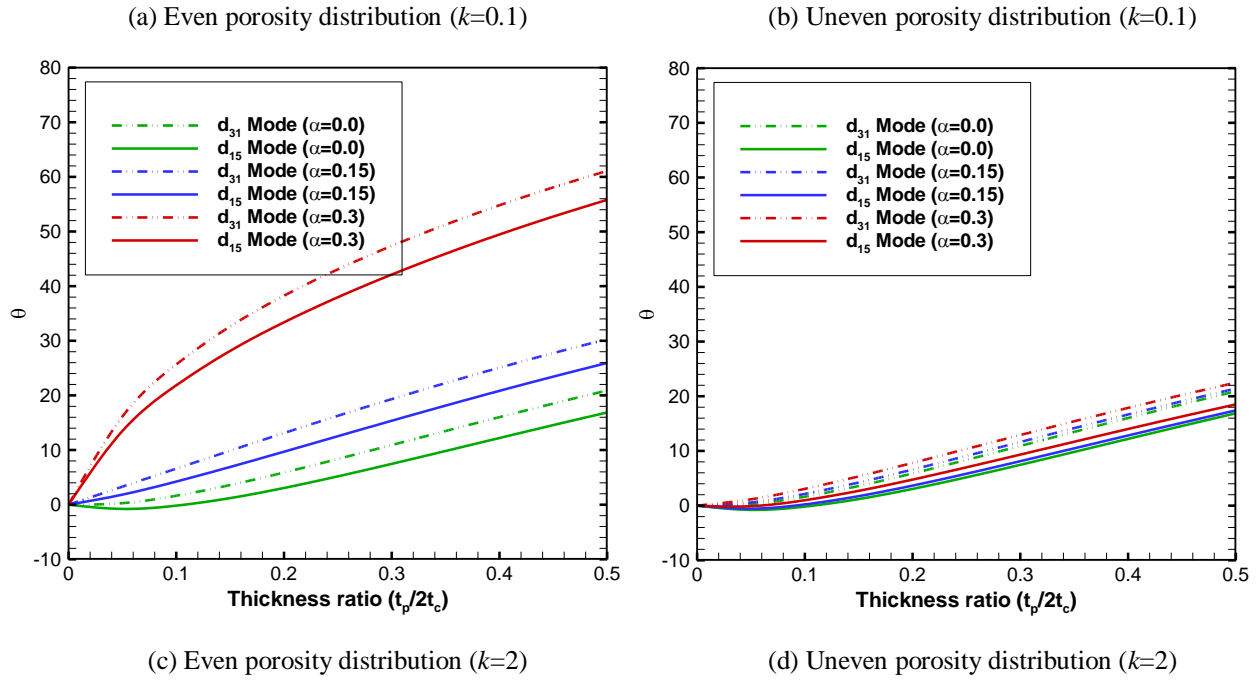
$$\theta = \frac{\omega|_{\text{With Piezo Layers}} - \omega|_{\text{Without Piezo Layers}}}{\omega|_{\text{Without Piezo Layers}}} \times 100 \tag{25}$$

For smart FGP beams with $L/2t_c$=15 and α=0.2, the variation of θ versus $t_p/2t_c$ is plotted in Figures 6(a) to 6(d). The figures reveal that, at a fixed value of $t_p/2t_c$, the value of θ is more sensitive to k for the beams with evenly distributed pores than that of the ones with uneven distribution. When k is small, the values of θ are negative regardless of the type of piezoelectric layers and porosity distribution, meaning that the coupled FGP beams have lower frequencies than the corresponding core beams. This behavior is due to the fact that the mass density of the material of piezoelectric layers (here PZT-5H) is greater than that of the considered material for the core layer, and consequently the effective mass density of the hybrid beam increases. Furthermore, the elastic modulus of the material of the core layer is higher than that of piezoelectric material, resulting in a decrease in the effective structural stiffness of the sandwich beam. On the other hand, when coupling piezoelectric layers with the core layer, the electromechanical coupling effect of piezoelectrics tends to increase the natural frequency of the hybrid structure, as concluded in the study of Wu et al.[54]. Thus, negative values of θ show that the electromechanical coupling effect of piezoelectric layers is less than that of the combined effects coming from the reduction in overall mass density and the growth in the effective stiffness. In addition, when the power-law index gets larger, the addition of piezoelectric layers results in opposite changes in the effective mass density and stiffness of the hybrid structure which finally leads to increase the natural frequencies, as seen from the curves corresponded to k=0.5, 1 and 5.

24

(a) Even porosity distribution – d_{31} Mode

(b) Even porosity distribution – d_{15} Mode

(c) Uneven porosity distribution – d_{31} Mode

(d) Uneven porosity distribution – d_{15} Mode

Figure 6. Variation of θ versus the thickness ratio for FGP beams coupled with d_{31} and d_{15} piezoelectric layers in SC condition ($L/2t_c$=15, α=0.2)

(a) Even porosity distribution (*k*=0.1)　　　　(b) Uneven porosity distribution (*k*=0.1)

(c) Even porosity distribution (*k*=2)　　　　(d) Uneven porosity distribution (*k*=2)

Figure 7. Variation of θ versus the thickness ratio for a FGP beam integrated with d_{31} and d_{15} piezoelectric layers in OC condition ($L/2t_c$=5)

In Figure 7, for different values of the porosity parameter 0, 0.15 and 0.3, and the power-law index 0.1 and 2, variations of θ versus $t_p/2t_c$ are depicted for the FGP beams with integrated d_{31} and d_{15} piezoelectric layers in OC electrical condition. Again, it is seen that the addition of both transverse and shear piezoelectric layers to FGP core beam has a greater effect on the natural frequencies when the internal pores are evenly distributed with respect to uneven distribution, regardless of the value of *k*. Moreover, by increasing the porosity volume fraction, the magnitude of θ increases for both even and uneven porosity distribution in such a way that this growth is more significant for the beam with even distribution and *k*=2 (see Figure 7(c)). It is also observed that when *k*=0.1, the magnitude of θ raises with an increase in the thickness of piezoelectric layers till $t_p/2t_c$=0.25; subsequently, the magnitude of θ drops as the value of $t_p/2t_c$ increases. It is due to the reason that when $t_p/2t_c$ is less than 0.25, the combined effects of the rise in the effective mass density and the fall in the structural stiffness are more than the increasing electromechanical effect due to increasing the piezoelectric layers' thickness. However, from $t_p/2t_c$=0.25 to 0.5, the trend of θ changes reversely, as the thickness ratio increases, meaning that the electromechanical effect overcomes the other two mentioned effects, which leads to the increasing trend of θ, as shown in Figures 7(a) and 7(b). By examining the numerical results, it is simple to acquire the similar conclusions for SC electrical boundary condition.

(a) Even porosity distribution   (b) Uneven porosity distribution
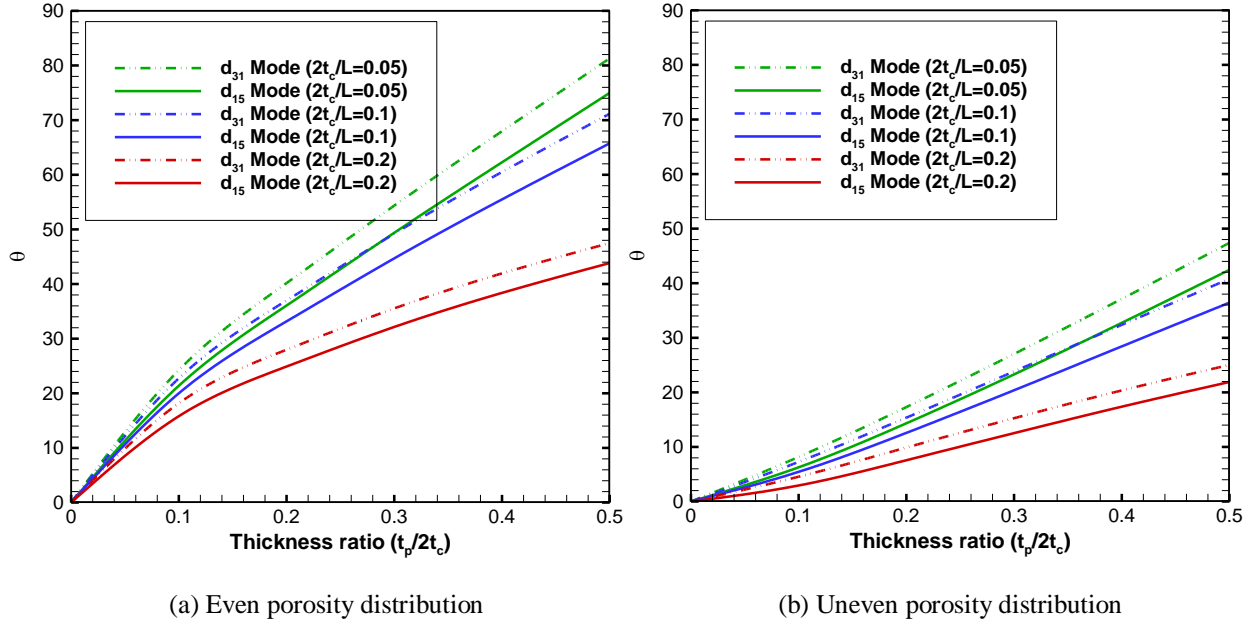
Figure 8. Variation of θ versus the thickness ratio for smart FGP beams in SC condition with different values of $L/2t_c$ ($k=5$, $\alpha=0.2$)

The last numerical example is provided in Figure (8) to show the effect of the piezoelectric layers' thickness on the SC fundamental frequency of FGP beams having $2t_c/L=0.05$, 0.1 and 0.2. As obvious, the value of θ decreases with an increase in the value of the core thickness for both d_{31} and d_{15} modes. It does mean that adding piezoelectric layers to FGP beams has a greater effect on the eigenfrequencies of the beams with lower core thickness.

7. Conclusion

In this article, employing various beam theories, an analytical approach has been developed to study the eigenfrequency behavior of simply supported smart FGP beams having different porosity distributions as well as various types of piezoelectric layers. The effects of material variation, porosity, beam dimensions, beam theories and piezoelectric characteristics on the resonance frequencies have been investigated in details. By analyzing the numerical simulations, the following conclusions are reached:

- FGP beams coupled with d_{15} piezoelectric layers provide lower resonant frequencies than the ones integrated with d_{31} piezoelectric layers;
- In d_{31} mode, the OC natural frequencies are greater than those of the SC condition, while there is virtually no difference between SC and OC frequencies when the FGP beam is surrounded by d_{15} piezoelectric layers;
- Adding piezoelectric layers has more effects on the eigenfrequencies when the internal pores are evenly distributed, and the changes in natural frequency due to adding piezoelectric layers is highly dependent upon the value of k;
- Variation of the eigenfrequencies versus porosity depends on the value of power-law index and the type of porosity distribution regardless of the piezoelectric characteristics;
- The smart FGP beams with unevenly distributed pores usually provide higher resonant frequencies than those of the beams with even porosity pattern;

27

- Increasing the power-law index *k* remarkably decrease the eigenfrequencies irrespective of the type of porosity pattern;
- The beam natural frequencies are more sensitive when the internal pores are evenly distributed.

Appendix: Definition of materials' coefficients

The coefficients a_i^{pq} ($i = 1, 2, \dots, 13$), β_i^{pq} ($i = 1, 2, \dots, 4$), and μ_i^{pq} ($i = 1, 2, \dots, 4$) in Transverse (d_{31}) Mode are defined as

In the SC electrical condition:

$$\begin{pmatrix} a_1^{31} \\ a_4^{31} \\ a_7^{31} \end{pmatrix} = \int_{-t_c-t_p}^{-t_c} \begin{pmatrix} 1 \\ z \\ f(z) \end{pmatrix} C_{11}\, dz + \int_{-t_c}^{+t_c} \begin{pmatrix} 1 \\ z \\ f(z) \end{pmatrix} Q_{11}\, dz + \int_{+t_c}^{+t_c+t_p} \begin{pmatrix} 1 \\ z \\ f(z) \end{pmatrix} C_{11}\, dz$$

$$\begin{pmatrix} a_2^{31} \\ a_5^{31} \\ a_8^{31} \end{pmatrix} = -\int_{-t_c-t_p}^{-t_c} \begin{pmatrix} 1 \\ z \\ f(z) \end{pmatrix} zC_{11}\, dz - \int_{-t_c}^{+t_c} \begin{pmatrix} 1 \\ z \\ f(z) \end{pmatrix} zQ_{11}\, dz - \int_{+t_c}^{+t_c+t_p} \begin{pmatrix} 1 \\ z \\ f(z) \end{pmatrix} zC_{11}\, dz$$

$$\begin{pmatrix} a_3^{31} \\ a_6^{31} \\ a_9^{31} \end{pmatrix} = \int_{-t_c-t_p}^{-t_c} \begin{pmatrix} 1 \\ z \\ f(z) \end{pmatrix} f(z)C_{11}\, dz + \int_{-t_c}^{+t_c} \begin{pmatrix} 1 \\ z \\ f(z) \end{pmatrix} f(z)Q_{11}\, dz + \int_{+t_c}^{+t_c+t_p} \begin{pmatrix} 1 \\ z \\ f(z) \end{pmatrix} f(z)C_{11}\, dz$$

$$a_{10}^{31} = \int_{-t_c-t_p}^{-t_c} [f'(z)]^2 C_{55}\, dz + \int_{-t_c}^{+t_c} [f'(z)]^2 Q_{55}\, dz + \int_{+t_c}^{+t_c+t_p} [f'(z)]^2 C_{55}\, dz$$

$$\begin{pmatrix} a_{11}^{31} \\ a_{12}^{31} \\ a_{13}^{31} \end{pmatrix} = \begin{pmatrix} 0 \\ 0 \\ 0 \end{pmatrix}$$

$$\begin{pmatrix} \mu_1^{31} \\ \mu_2^{31} \\ \mu_3^{31} \end{pmatrix} = \int_{-t_c-t_p}^{-t_c} \begin{pmatrix} 1 \\ z \\ f(z) \end{pmatrix} \frac{4e_{31}}{t_p}\left[\frac{-2z - 2t_c - t_p}{t_p}\right] dz - \int_{+t_c}^{+t_c+t_p} \begin{pmatrix} 1 \\ z \\ f(z) \end{pmatrix} \frac{4e_{31}}{t_p}\left[\frac{2z - 2t_c - t_p}{t_p}\right] dz$$

$$\mu_4^{31} = 0$$

$$\mu_5^{31} = \int_{-t_c-t_p}^{-t_c} \frac{8\Xi_{33}}{(t_p)^2}\, dz + \int_{+t_c}^{+t_c+t_p} \frac{8\Xi_{33}}{(t_p)^2}\, dz$$

$$\begin{pmatrix} \beta_1^{31} \\ \beta_2^{31} \\ \beta_3^{31} \end{pmatrix} = \begin{pmatrix} 0 \\ 0 \\ 0 \end{pmatrix}$$

$$\beta_4^{31} = \int_{-t_c-t_p}^{-t_c} f'(z)\, e_{15} \left[1 - \left(\frac{-2z - 2t_c - t_p}{t_p} \right)^2 \right] dz$$

$$+ \int_{+t_c}^{+t_c+t_p} f'(z)\, e_{15} \left[1 - \left(\frac{2z - 2t_c - t_p}{t_p} \right)^2 \right] dz$$

$$\beta_5^{31} = -\int_{-t_c-t_p}^{-t_c} \Xi_{11} \left[1 - \left(\frac{-2z - 2t_c - t_p}{t_p} \right)^2 \right] dz - \int_{+t_c}^{+t_c+t_p} \Xi_{11} \left[1 - \left(\frac{2z - 2t_c - t_p}{t_p} \right)^2 \right] dz$$

$$\begin{pmatrix} b_1^{31} \\ b_3^{31} \\ b_4^{31} \\ b_5^{31} \\ b_6^{31} \\ b_8^{31} \\ b_9^{31} \end{pmatrix} = \begin{pmatrix} 0 \\ 0 \\ 0 \\ 0 \\ 0 \\ 0 \\ 0 \end{pmatrix}$$

$$b_2^{31} = \int_{-t_c-t_p}^{-t_c} f'(z)(e_{31} + e_{15})\, dz + \int_{+t_c}^{+t_c+t_p} f'(z)(e_{31} + e_{15})\, dz$$

$$b_7^{31} = -\int_{-t_c-t_p}^{-t_c} e_{31}\, dz - \int_{+t_c}^{+t_c+t_p} e_{31}\, dz \tag{A.1}$$

In the OC electrical condition:

$$\begin{pmatrix} a_1^{31} \\ a_4^{31} \\ a_7^{31} \end{pmatrix} = \int_{-t_c-t_p}^{-t_c} \begin{pmatrix} 1 \\ z \\ f(z) \end{pmatrix} \left[C_{11} + \frac{e_{31}^2}{\Xi_{33}} \right] dz + \int_{-t_c}^{+t_c} \begin{pmatrix} 1 \\ z \\ f(z) \end{pmatrix} Q_{11}\, dz$$

$$+ \int_{+t_c}^{+t_c+t_p} \begin{pmatrix} 1 \\ z \\ f(z) \end{pmatrix} \left[C_{11} + \frac{e_{31}^2}{\Xi_{33}} \right] dz$$

$$\begin{pmatrix} a_2^{31} \\ a_5^{31} \\ a_8^{31} \end{pmatrix} = \int_{-t_c-t_p}^{-t_c} \begin{pmatrix} 1 \\ z \\ f(z) \end{pmatrix} \left[-zC_{11} + \frac{(t_c + t_p)e_{31}^2}{\Xi_{33}} \right] dz - \int_{-t_c}^{+t_c} \begin{pmatrix} 1 \\ z \\ f(z) \end{pmatrix} zQ_{11}\, dz$$

$$+ \int_{+t_c}^{+t_c+t_p} \begin{pmatrix} 1 \\ z \\ f(z) \end{pmatrix} \left[-zC_{11} + \frac{(t_c + t_p)e_{31}^2}{\Xi_{33}} \right] dz$$

$$\begin{pmatrix} a_3^{31} \\ a_6^{31} \\ a_9^{31} \end{pmatrix} = \int_{-t_c-t_p}^{-t_c} \begin{pmatrix} 1 \\ z \\ f(z) \end{pmatrix} \left[f(z)C_{11} + \frac{\eta_2 e_{31}^2}{\Xi_{33}} \right] dz + \int_{-t_c}^{+t_c} \begin{pmatrix} 1 \\ z \\ f(z) \end{pmatrix} f(z)Q_{11}\, dz$$

$$+ \int_{+t_c}^{+t_c+t_p} \begin{pmatrix} 1 \\ z \\ f(z) \end{pmatrix} \left[f(z)C_{11} + \frac{\eta_1 e_{31}^2}{\Xi_{33}} \right] dz$$

$$a_{10}^{31} = \int_{-t_c-t_p}^{-t_c} [f'(z)]^2 C_{55}\, dz + \int_{-t_c}^{+t_c} [f'(z)]^2 Q_{55}\, dz + \int_{+t_c}^{+t_c+t_p} [f'(z)]^2 C_{55}\, dz$$

$$\begin{pmatrix} a_{11}^{31} \\ a_{12}^{31} \\ a_{13}^{31} \end{pmatrix} = \int_{-t_c-t_p}^{-t_c} \begin{pmatrix} \eta_2 \\ 1 \\ t_c + t_p \end{pmatrix} \frac{f'(z)e_{15}e_{31}(z+t_c)}{\Xi_{33}}\, dz + \int_{+t_c}^{+t_c+t_p} \begin{pmatrix} \eta_1 \\ 1 \\ t_c + t_p \end{pmatrix} \frac{f'(z)e_{15}e_{31}(z-t_c)}{\Xi_{33}}\, dz$$

$$\begin{pmatrix} \mu_1^{31} \\ \mu_2^{31} \\ \mu_3^{31} \end{pmatrix} = -\int_{-t_c-t_p}^{-t_c} \begin{pmatrix} 1 \\ z \\ f(z) \end{pmatrix} \frac{8e_{31}}{t_p}(z+t_c+t_p)\, dz - \int_{+t_c}^{+t_c+t_p} \begin{pmatrix} 1 \\ z \\ f(z) \end{pmatrix} \frac{8e_{31}}{t_p}(z-t_c-t_p)\, dz$$

$$\mu_4^{31} = 0$$

$$\mu_5^{31} = \int_{-t_c-t_p}^{-t_c} \frac{8\Xi_{33}}{(t_p)^2}\, dz + \int_{+t_c}^{+t_c+t_p} \frac{8\Xi_{33}}{(t_p)^2}\, dz$$

$$\begin{pmatrix} \beta_1^{31} \\ \beta_2^{31} \\ \beta_3^{31} \end{pmatrix} = \begin{pmatrix} 0 \\ 0 \\ 0 \end{pmatrix}$$

$$\beta_4^{31} = \int_{-t_c-t_p}^{-t_c} f'(z)\, e_{15}\left[1 - \left(\frac{-2z-2t_c-t_p}{t_p}\right)^2 - \frac{4(z+t_c)}{t_p}\right] dz$$
$$+ \int_{+t_c}^{+t_c+t_p} f'(z)\, e_{15}\left[1 - \left(\frac{2z-2t_c-t_p}{t_p}\right)^2 + \frac{4(z-t_c)}{t_p}\right] dz$$

$$\beta_5^{31} = -\int_{-t_c-t_p}^{-t_c} \Xi_{11}\left[1 - \left(\frac{-2z-2t_c-t_p}{t_p}\right)^2 - \frac{4(z+t_c)}{t_p}\right] dz$$
$$- \int_{+t_c}^{+t_c+t_p} \Xi_{11}\left[1 - \left(\frac{2z-2t_c-t_p}{t_p}\right)^2 + \frac{4(z-t_c)}{t_p}\right] dz$$

$$\begin{pmatrix} b_1^{31} \\ b_3^{31} \\ b_5^{31} \\ b_8^{31} \end{pmatrix} = \begin{pmatrix} 0 \\ 0 \\ 0 \\ 0 \end{pmatrix}$$

$$b_2^{31} = \int_{-t_c-t_p}^{-t_c} f'(z)(e_{31} + e_{15})\, dz + \int_{+t_c}^{+t_c+t_p} f'(z)(e_{31} + e_{15})\, dz$$

$$\begin{pmatrix} b_4^{31} \\ b_6^{31} \\ b_9^{31} \end{pmatrix} = -\int_{-t_c-t_p}^{-t_c} \begin{pmatrix} \eta_2 \\ 1 \\ t_c + t_p \end{pmatrix} \frac{\Xi_{11}e_{31}(z+t_c)}{\Xi_{33}}\, dz - \int_{+t_c}^{+t_c+t_p} \begin{pmatrix} \eta_1 \\ 1 \\ -t_c - t_p \end{pmatrix} \frac{\Xi_{11}e_{31}(z-t_c)}{\Xi_{33}}\, dz$$

$$b_7^{31} = -\int_{-t_c-t_p}^{-t_c} e_{31}\, dz - \int_{+t_c}^{+t_c+t_p} e_{31}\, dz \tag{A.2}$$

The coefficients a_i^{pq} $(i = 1, 2, ..., 13)$, β_i^{pq} $(i = 1, 2, ..., 4)$, and μ_i^{pq} $(i = 1, 2, ..., 4)$ in Shear (d_{15}) Mode are defined as

In the SC electrical condition:

$$\begin{pmatrix} a_1^{15} \\ a_4^{15} \\ a_7^{15} \end{pmatrix} = \int_{-t_c-t_p}^{-t_c} \begin{pmatrix} 1 \\ z \\ f(z) \end{pmatrix} C_{33}\, dz + \int_{-t_c}^{+t_c} \begin{pmatrix} 1 \\ z \\ f(z) \end{pmatrix} Q_{11}\, dz + \int_{+t_c}^{+t_c+t_p} \begin{pmatrix} 1 \\ z \\ f(z) \end{pmatrix} C_{33}\, dz$$

$$\begin{pmatrix} a_2^{15} \\ a_5^{15} \\ a_8^{15} \end{pmatrix} = -\int_{-t_c-t_p}^{-t_c} \begin{pmatrix} 1 \\ z \\ f(z) \end{pmatrix} zC_{33}\, dz - \int_{-t_c}^{+t_c} \begin{pmatrix} 1 \\ z \\ f(z) \end{pmatrix} zQ_{11}\, dz - \int_{+t_c}^{+t_c+t_p} \begin{pmatrix} 1 \\ z \\ f(z) \end{pmatrix} zC_{33}\, dz$$

$$\begin{pmatrix} a_3^{15} \\ a_6^{15} \\ a_9^{15} \end{pmatrix} = \int_{-t_c-t_p}^{-t_c} \begin{pmatrix} 1 \\ z \\ f(z) \end{pmatrix} f(z)C_{33}\, dz + \int_{-t_c}^{+t_c} \begin{pmatrix} 1 \\ z \\ f(z) \end{pmatrix} f(z)Q_{11}\, dz + \int_{+t_c}^{+t_c+t_p} \begin{pmatrix} 1 \\ z \\ f(z) \end{pmatrix} f(z)C_{33}\, dz$$

$$a_{10}^{15} = \int_{-t_c-t_p}^{-t_c} [f'(z)]^2 C_{55}\, dz + \int_{-t_c}^{+t_c} [f'(z)]^2 Q_{55}\, dz + \int_{+t_c}^{+t_c+t_p} [f'(z)]^2 C_{55}\, dz$$

$$\begin{pmatrix} a_{11}^{15} \\ a_{12}^{15} \\ a_{13}^{15} \end{pmatrix} = \begin{pmatrix} 0 \\ 0 \\ 0 \end{pmatrix}$$

$$\begin{pmatrix} \mu_1^{15} \\ \mu_2^{15} \\ \mu_3^{15} \end{pmatrix} = \begin{pmatrix} 0 \\ 0 \\ 0 \end{pmatrix}$$

$$\mu_4^{15} = \int_{-t_c-t_p}^{-t_c} \frac{4e_{15}f'(z)}{t_p}\left[\frac{-2z - 2t_c - t_p}{t_p}\right] dz - \int_{+t_c}^{+t_c+t_p} \frac{4e_{15}f'(z)}{t_p}\left[\frac{2z - 2t_c - t_p}{t_p}\right] dz$$

$$\mu_5^{15} = \int_{-t_c-t_p}^{-t_c} \frac{8\Xi_{11}}{(t_p)^2}\, dz + \int_{+t_c}^{+t_c+t_p} \frac{8\Xi_{11}}{(t_p)^2}\, dz$$

$$\begin{pmatrix} \beta_1^{15} \\ \beta_2^{15} \\ \beta_3^{15} \end{pmatrix} = \int_{-t_c-t_p}^{-t_c} \begin{pmatrix} 1 \\ z \\ f(z) \end{pmatrix} e_{33}\left[1 - \left(\frac{-2z - 2t_c - t_p}{t_p}\right)^2\right] dz$$

$$+ \int_{+t_c}^{+t_c+t_p} \begin{pmatrix} 1 \\ z \\ f(z) \end{pmatrix} e_{33}\left[1 - \left(\frac{2z - 2t_c - t_p}{t_p}\right)^2\right] dz$$

$$\beta_4^{15} = 0$$

$$\beta_5^{15} = -\int_{-t_c-t_p}^{-t_c} \Xi_{33}\left[1 - \left(\frac{-2z - 2t_c - t_p}{t_p}\right)^2\right] dz - \int_{+t_c}^{+t_c+t_p} \Xi_{33}\left[1 - \left(\frac{2z - 2t_c - t_p}{t_p}\right)^2\right] dz$$

$$\begin{pmatrix} b_2^{15} \\ b_4^{15} \\ b_6^{15} \\ b_7^{15} \\ b_9^{15} \end{pmatrix} = \begin{pmatrix} 0 \\ 0 \\ 0 \\ 0 \\ 0 \end{pmatrix}$$

$$b_1^{15} = \int_{-t_c-t_p}^{-t_c} e_{15} f''(z)\, dz + \int_{+t_c}^{+t_c+t_p} e_{15} f''(z)\, dz$$

$$b_3^{15} = \int_{-t_c-t_p}^{-t_c} e_{33} f(z)\, dz + \int_{+t_c}^{+t_c+t_p} e_{33} f(z)\, dz$$

$$b_5^{15} = \int_{-t_c-t_p}^{-t_c} e_{33}\, dz + \int_{+t_c}^{+t_c+t_p} e_{33}\, dz$$

$$b_8^{15} = -\int_{-t_c-t_p}^{-t_c} z e_{31}\, dz - \int_{+t_c}^{+t_c+t_p} z e_{31}\, dz \tag{A.3}$$

In the OC electrical condition:

$$\begin{pmatrix} a_1^{15} \\ a_4^{15} \\ a_7^{15} \end{pmatrix} = \int_{-t_c-t_p}^{-t_c} \begin{pmatrix} 1 \\ z \\ f(z) \end{pmatrix} C_{33}\, dz + \int_{-t_c}^{+t_c} \begin{pmatrix} 1 \\ z \\ f(z) \end{pmatrix} Q_{11}\, dz + \int_{+t_c}^{+t_c+t_p} \begin{pmatrix} 1 \\ z \\ f(z) \end{pmatrix} C_{33}\, dz$$

$$\begin{pmatrix} a_2^{15} \\ a_5^{15} \\ a_8^{15} \end{pmatrix} = -\int_{-t_c-t_p}^{-t_c} \begin{pmatrix} 1 \\ z \\ f(z) \end{pmatrix} z C_{33}\, dz - \int_{-t_c}^{+t_c} \begin{pmatrix} 1 \\ z \\ f(z) \end{pmatrix} z Q_{11}\, dz - \int_{+t_c}^{+t_c+t_p} \begin{pmatrix} 1 \\ z \\ f(z) \end{pmatrix} z C_{33}\, dz$$

$$\begin{pmatrix} a_3^{15} \\ a_6^{15} \\ a_9^{15} \end{pmatrix} = \int_{-t_c-t_p}^{-t_c} \begin{pmatrix} 1 \\ z \\ f(z) \end{pmatrix} \left[C_{33} f(z) + \frac{e_{15} e_{33} \zeta_2 (z + t_c)}{\Xi_{11}} \right] dz + \int_{-t_c}^{+t_c} \begin{pmatrix} 1 \\ z \\ f(z) \end{pmatrix} f(z) Q_{11}\, dz$$

$$+ \int_{+t_c}^{+t_c+t_p} \begin{pmatrix} 1 \\ z \\ f(z) \end{pmatrix} \left[C_{33} f(z) + \frac{e_{15} e_{33} \zeta_1 (z - t_c)}{\Xi_{11}} \right] dz$$

$$a_{10}^{15} = \int_{-t_c-t_p}^{-t_c} \left(C_{55} [f'(z)]^2 + \frac{\zeta_2 f'(z) e_{15}{}^2}{\Xi_{11}} \right) dz + \int_{-t_c}^{+t_c} Q_{55} [f'(z)]^2\, dz$$

$$+ \int_{+t_c}^{+t_c+t_p} \left(C_{55} [f'(z)]^2 + \frac{\zeta_1 f'(z) e_{15}{}^2}{\Xi_{11}} \right) dz$$

$$\begin{pmatrix} a_{11}^{15} \\ a_{12}^{15} \\ a_{13}^{15} \end{pmatrix} = \begin{pmatrix} 0 \\ 0 \\ 0 \end{pmatrix}$$

$$\begin{pmatrix} \mu_1^{15} \\ \mu_2^{15} \\ \mu_3^{15} \end{pmatrix} = \begin{pmatrix} 0 \\ 0 \\ 0 \end{pmatrix}$$

$$\mu_4^{15} = -\int_{-t_c-t_p}^{-t_c} \frac{8e_{15}f'(z)}{t_p}\left[\frac{z+t_c+t_p}{t_p}\right]dz - \int_{+t_c}^{+t_c+t_p} \frac{8e_{15}f'(z)}{t_p}\left[\frac{z-t_c-t_p}{t_p}\right]dz$$

$$\mu_5^{15} = \int_{-t_c-t_p}^{-t_c} \frac{8\Xi_{11}}{(t_p)^2}dz + \int_{+t_c}^{+t_c+t_p} \frac{8\Xi_{11}}{(t_p)^2}dz$$

$$\begin{pmatrix} \beta_1^{15} \\ \beta_2^{15} \\ \beta_3^{15} \end{pmatrix} = \int_{-t_c-t_p}^{-t_c} \begin{pmatrix} 1 \\ z \\ f(z) \end{pmatrix} e_{33}\left[1-\left(\frac{-2z-2t_c-t_p}{t_p}\right)^2 - \frac{4(z+t_c)}{t_p}\right]dz$$

$$+ \int_{+t_c}^{+t_c+t_p} \begin{pmatrix} 1 \\ z \\ f(z) \end{pmatrix} e_{33}\left[1-\left(\frac{2z-2t_c-t_p}{t_p}\right)^2 + \frac{4(z-t_c)}{t_p}\right]dz$$

$$\beta_4^{15} = 0$$

$$\beta_5^{15} = -\int_{-t_c-t_p}^{-t_c} \Xi_{33}\left[1-\left(\frac{-2z-2t_c-t_p}{t_p}\right)^2 - \frac{4(z+t_c)}{t_p}\right]dz$$

$$-\int_{+t_c}^{+t_c+t_p} \Xi_{33}\left[1-\left(\frac{2z-2t_c-t_p}{t_p}\right)^2 + \frac{4(z-t_c)}{t_p}\right]dz$$

$$\begin{pmatrix} b_2^{15} \\ b_4^{15} \\ b_6^{15} \\ b_7^{15} \\ b_9^{15} \end{pmatrix} = \begin{pmatrix} 0 \\ 0 \\ 0 \\ 0 \\ 0 \end{pmatrix}$$

$$b_1^{15} = \int_{-t_c-t_p}^{-t_c} e_{15}f''(z)\,dz + \int_{+t_c}^{+t_c+t_p} e_{15}f''(z)\,dz$$

$$b_3^{15} = \int_{-t_c-t_p}^{-t_c} \left(e_{33}f(z) - \frac{e_{15}\zeta_2\Xi_{33}(z+t_c)}{\Xi_{11}}\right)dz + \int_{+t_c}^{+t_c+t_p} \left(e_{33}f(z) - \frac{e_{15}\zeta_1\Xi_{33}(z-t_c)}{\Xi_{11}}\right)dz$$

$$b_5^{15} = \int_{-t_c-t_p}^{-t_c} e_{33}\,dz + \int_{+t_c}^{+t_c+t_p} e_{33}\,dz$$

$$b_8^{15} = -\int_{-t_c-t_p}^{-t_c} ze_{33}\,dz - \int_{+t_c}^{+t_c+t_p} ze_{33}\,dz \tag{A.4}$$

8. References

1.   Miyamoto Y, Kaysser WA, Rabin BH, et al. *Functionally graded materials: design, processing and applications.* Springer Science & Business Media, 2013.

2.   Jha DK, Kant T and Singh RK. A critical review of recent research on functionally graded plates. *Composite Structures* 2013; 96: 833-849.

3.   Qatu MS. *Vibration of laminated shells and plates*. Elsevier, 2004.

4.   Ying J, Lü CF and Chen WQ. Two-dimensional elasticity solutions for functionally graded beams resting on elastic foundations. *Composite Structures* 2008; 84: 209-219.

5.   Xu YP and Zhou D. Three-dimensional elasticity solution of simply supported functionally graded rectangular plates with internal elastic line supports. *The Journal of Strain Analysis for Engineering Design* 2009; 44: 249-261.

6.   Huang Y and Li XF. A new approach for free vibration of axially functionally graded beams with non-uniform cross-section. *Journal of sound and vibration* 2010; 329: 2291-2303.

7.   Ke LL, Yang J and Kitipornchai S. An analytical study on the nonlinear vibration of functionally graded beams. *Meccanica* 2010; 45: 743-752.

8.   Alshorbagy AE, Eltaher MA and Mahmoud FF. Free vibration characteristics of a functionally graded beam by finite element method. *Applied Mathematical Modelling* 2011; 35: 412-425.

9.   Pradhan KK and Chakraverty S. Free vibration of Euler and Timoshenko functionally graded beams by Rayleigh–Ritz method. *Composites Part B: Engineering* 2013; 51: 175-184.

10.   Chakraverty S and Pradhan KK. *Vibration of functionally graded beams and plates*. Academic Press, 2016.

11.   Wang Q, Shi D, Liang Q, et al. A unified solution for vibration analysis of functionally graded circular, annular and sector plates with general boundary conditions. *Composites Part B: Engineering* 2016; 88: 264-294.

12.   Paul A and Das D. A study on non-linear post-buckling behavior of tapered Timoshenko beam made of functionally graded material under in-plane thermal loadings. *The Journal of Strain Analysis for Engineering Design* 2017; 52: 45-56.

13.   Wang YQ and Zu JW. Nonlinear dynamics of functionally graded material plates under dynamic liquid load and with longitudinal speed. *International Journal of Applied Mechanics* 2017; 9: 1750054.

14.   Paul A and Das D. Non-linear forced vibration analysis of higher-order shear-deformable functionally graded material beam in thermal environment subjected to harmonic excitation and resting on non-linear elastic foundation. *The Journal of Strain Analysis for Engineering Design* 2018; 53: 446-462.

15.   Wang YQ and Zu JW. Nonlinear dynamics of a translational FGM plate with strong mode interaction. *International Journal of Structural Stability and Dynamics* 2018; 18: 1850031.

16.   Burlayenko VN and Sadowski T. Free vibrations and static analysis of functionally graded sandwich plates with three-dimensional finite elements. *Meccanica* 2019: 1-18.

17.   Zhu J, Lai Z, Yin Z, et al. Fabrication of ZrO_2–NiCr functionally graded material by powder metallurgy. *Materials Chemistry and Physics* 2001; 68: 130-135.

18.   Wattanasakulpong N, Prusty BG, Kelly DW, et al. Free vibration analysis of layered functionally graded beams with experimental validation. *Materials & Design (1980-2015)* 2012; 36: 182-190.

19.   Chen D, Yang J and Kitipornchai S. Elastic buckling and static bending of shear deformable functionally graded porous beam. *Composite Structures* 2015; 133: 54-61.

20.   Chen D, Kitipornchai S and Yang J. Nonlinear free vibration of shear deformable sandwich beam with a functionally graded porous core. *Thin-Walled Structures* 2016; 107: 39-48.

21.   Ebrahimi F, Ghasemi F and Salari E. Investigating thermal effects on vibration behavior of temperature-dependent compositionally graded Euler beams with porosities. *Meccanica* 2016; 51: 223-249.

22.   Ebrahimi F and Jafari A. A four-variable refined shear-deformation beam theory for thermo-mechanical vibration analysis of temperature-dependent FGM beams with porosities. *Mechanics of Advanced Materials and Structures* 2018; 25: 212-224.

23.   Ebrahimi F, Dabbagh A and Rastgoo A. Vibration analysis of porous metal foam shells rested on an elastic substrate. *The Journal of Strain Analysis for Engineering Design* 2019: 0309324719852555.

24.   Wang YQ and Yang Z. Nonlinear vibrations of moving functionally graded plates containing porosities and contacting with liquid: internal resonance. *Nonlinear Dynamics* 2017; 90: 1461-1480.

25.   Wang YQ and Zu JW. Vibration behaviors of functionally graded rectangular plates with porosities and moving in thermal environment. *Aerospace Science and Technology* 2017; 69: 550-562.

26.   Wang YQ and Zu JW. Porosity-dependent nonlinear forced vibration analysis of functionally graded piezoelectric smart material plates. *Smart Materials and structures* 2017; 26: 105014.

27.   Wang YQ, Ye C and Zu JW. Nonlinear vibration of metal foam cylindrical shells reinforced with graphene platelets. *Aerospace Science and Technology* 2019; 85: 359-370.

28.	Zenkour AM. A quasi-3D refined theory for functionally graded single-layered and sandwich plates with porosities. *Composite Structures* 2018; 201: 38-48.

29.	Nguyen NV, Nguyen HX, Lee S, et al. Geometrically nonlinear polygonal finite element analysis of functionally graded porous plates. *Advances in Engineering Software* 2018; 126: 110-126.

30.	Wang YQ and Zhao HL. Bending, buckling and vibration of shear deformable beams made of three-dimensional graphene foam material. *Journal of the Brazilian Society of Mechanical Sciences and Engineering* 2019; 41: 422.

31.	Cao L, Mantell S and Polla D. Design and simulation of an implantable medical drug delivery system using microelectromechanical systems technology. *Sensors and Actuators A: Physical* 2001; 94: 117-125.

32.	He XQ, Ng TY, Sivashanker S, et al. Active control of FGM plates with integrated piezoelectric sensors and actuators. *International journal of Solids and Structures* 2001; 38: 1641-1655.

33.	Ray MC. Optimal control of laminated shells using piezoelectric sensor and actuator layers. *AIAA Journal* 2003; 41: 1151-1157.

34.	Peng F, Ng A and Hu YR. Actuator placement optimization and adaptive vibration control of plate smart structures. *Journal of Intelligent Material Systems and Structures* 2005; 16: 263-271.

35.	Yang Z, Zhou S, Zu J, et al. High-performance piezoelectric energy harvesters and their applications. *Joule* 2018; 2: 642-697.

36.	Ebrahimi F. Piezoelectric Actuators for Functionally Graded Plates-Nonlinear Vibration Analysis. *Piezoelectric Materials and Devices-Practice and Applications*. IntechOpen, 2013.

37.	Zhang SQ and Schmidt R. Static and dynamic FE analysis of piezoelectric integrated thin-walled composite structures with large rotations. *Composite Structures* 2014; 112: 345-357.

38.	Zhang SQ, Li YX and Schmidt R. Modeling and simulation of macro-fiber composite layered smart structures. *Composite Structures* 2015; 126: 89-100.

39.	Zhang SQ, Li YX and Schmidt R. Active shape and vibration control for piezoelectric bonded composite structures using various geometric nonlinearities. *Composite Structures* 2015; 122: 239-249.

40.	Reddy JN and Cheng ZQ. Three-dimensional solutions of smart functionally graded plates. *J Appl Mech* 2000; 68: 234-241.

41.	Wang BL and Noda N. Design of a smart functionally graded thermopiezoelectric composite structure. *Smart Materials and Structures* 2001; 10: 189.

42.	Huang XL and Shen HS. Vibration and dynamic response of functionally graded plates with piezoelectric actuators in thermal environments. *Journal of Sound and Vibration* 2006; 289: 25-53.

43.	Kiani Y, Rezaei M, Taheri S, et al. Thermo-electrical buckling of piezoelectric functionally graded material Timoshenko beams. *International Journal of Mechanics and Materials in Design* 2011; 7: 185-197.

44.	Askari Farsangi MA and Saidi AR. Levy type solution for free vibration analysis of functionally graded rectangular plates with piezoelectric layers. *Smart Materials and Structures* 2012; 21: 094017.

45.	Askari Farsangi MA, Saidi AR and Batra RC. Analytical solution for free vibrations of moderately thick hybrid piezoelectric laminated plates. *Journal of Sound and Vibration* 2013; 332: 5981-5998.

46.	Wang YQ. Electro-mechanical vibration analysis of functionally graded piezoelectric porous plates in the translation state. *Acta Astronautica* 2018; 143: 263-271.

47.	Wang YQ, Wan YH and Zhang YF. Vibrations of longitudinally traveling functionally graded material plates with porosities. *European Journal of Mechanics-A/Solids* 2017; 66: 55-68.

48.	Wang YQ and Zu JW. Vibration characteristics of moving sigmoid functionally graded plates containing porosities. *International Journal of Mechanics and Materials in Design* 2018; 14: 473-489.

49.	Wattanasakulpong N and Chaikittiratana A. Flexural vibration of imperfect functionally graded beams based on Timoshenko beam theory: Chebyshev collocation method. *Meccanica* 2015; 50: 1331-1342.

50.	Malakooti MH and Sodano HA. Piezoelectric energy harvesting through shear mode operation. *Smart Materials and Structures* 2015; 24: 055005.

51.	Sobhy M. Buckling and free vibration of exponentially graded sandwich plates resting on elastic foundations under various boundary conditions. *Composite Structures* 2013; 99: 76-87.

52.	Yang J. *Special topics in the theory of piezoelectricity*. Springer Science & Business Media, 2010.

53.	Wang Q, Quek ST, Sun CT, et al. Analysis of piezoelectric coupled circular plate. *Smart Materials and Structures* 2001; 10: 229.

54.	Wu N, Wang Q and Quek S. Free vibration analysis of piezoelectric coupled circular plate with open circuit. *Journal of Sound and Vibration* 2010; 329: 1126-1136.

55.	Askari M, Brusa E and Delprete C. Electromechanical Vibration Characteristics of Porous Bimorph and Unimorph Doubly Curved Panels. In: *Actuators* 2020, p.7. Multidisciplinary Digital Publishing Institute.

56. Aydogdu M and Taskin V. Free vibration analysis of functionally graded beams with simply supported edges. *Materials & design* 2007; 28: 1651-1656.

57. Su H, Banerjee J and Cheung C. Dynamic stiffness formulation and free vibration analysis of functionally graded beams. *Composite Structures* 2013; 106: 854-862.

58. Sayyaadi H and Rahnama F. On the energy harvesting via doubly curved piezoelectric panels. *Journal of Intelligent Material Systems and Structures* 2016; 27: 2692-2706.